

Homogenization of discrete mesoscale model of concrete for coupled mass transport and mechanics by asymptotic expansion

Jan Eliáš*[†]

Gianluca Cusatis[‡]

Abstract

Mass transport phenomenon in concrete structures is strongly coupled with their mechanical behavior. The first coupling fabric is the Biot's theory according to which fluid pressure interacts with solid stress state and volumetric deformation rate of the solid induces changes in fluid pressure. Another coupling mechanism emerges with cracks which serve as channels for the fluid to flow through them and provide volume for fluid storage. Especially the second coupling mechanism presents a challenge for numerical modeling as it requires detailed knowledge about cracking process. Discrete mesoscale mechanical models coupled with mass transport offer simple and robust way to solve the problem. On the other hand, however, they are computationally demanding.

In order to reduce this computational burden, the present paper applies the asymptotic expansion homogenization technique to the coupled problem to deliver (i) continuous and homogeneous description of the macroscopic problem which can be easily solved by the finite element method, (ii) discrete and heterogeneous mesoscale problem in the periodic setup attached to each integration point of the macroscale along with (iii) equations providing communication between these two scales. The transient terms appear at the macroscale only, as well as the Biot's coupling terms. The coupling through cracking is treated at the mesoscale by changing conductivity of the conduit elements according to the mechanical solution, otherwise the two mesoscale steady state problems are decoupled and can be therefore solved in a sequence. This paper presents verification studies showing performance of the homogenized solution. Further improvement is achieved by pre-computing the initial linear mesoscale solution and adaptively replacing it by the full nonlinear one only at integration points that fulfill Ottosen's stress-based criterion indicating deviation from linearity.

1 Introduction

Reliable, safe and efficient design of concrete structures demands robust numerical models capable to predict structural behavior under various external conditions, including post-critical stages. Coupled multi-physical phenomena are being commonly investigated in design and assessment of long term behavior and durability of concrete structures. One of the most frequent coupled analysis is a problem of mechanics and mass transport, which is the subject of investigation in the present paper.

Coupled mechanics and mass transport in porous quasibrittle medium is nowadays almost exclusively solved with a help of complex numerical models. Coupling is provided by the Biot's theory [9] where fluid pressure depends on volumetric deformation rate and solid stress state is affected by the fluid pressure. In addition, there is the a coupling source due to presence of cracks which create additional volume for fluid storage and increase material permeability. One can find several coupled simulation methods treating the material as homogeneous, such as X-FEM [54, 71] or phase-field [49, 73] techniques. The homogeneous approaches suffer from oversimplified representation of cracks and consequently less accurate capturing of the coupling effects.

Fracture process in quasibrittle materials is a complex and challenging problem. Research has demonstrated that it is advantageous to use mesoscale techniques that, by capturing features of the internal structure, provide accurate insight into the cracking state [59, 74]. Thereby, mesoscale models provide better estimation of flux through the cracks, i.e., more accurate description of the coupling effects. There is, however, a price paid for the quality of the results

*Brno University of Technology, Faculty of Civil Engineering, Brno, Czechia

[†]Corresponding author: jan.elias@vut.cz

[‡]Northwestern University, Department of Civil and Environmental Engineering, Evanston, IL USA

in a form of computational burden associated with mesoscale models. A partial reduction of this obstacle can be achieved by using discrete models where each numerical particle corresponds to a large inclusion with a surrounding matrix [22, 5, 28]. This not only drastically reduces the number of free parameters of the displacement field (called Degrees of Freedom or DoF hereinafter), it also brings several other advantages such as natural description of oriented and discontinuous cracks and simple vectorial form of constitutive equations [11]. On the other hand, there is also a disadvantage in a limited range of achievable Poisson’s ratio of the discrete system [22, 27, 11].

The mechanical discrete models have been extended by coupled multi-physical phenomena in the last two decades, the focus is placed on mass transport in particular. Initially, the transport problem was solved on the same discrete structure as mechanics, which brought difficulties in coupling flow with crack openings as the cracks were perpendicular to the conduit elements [10]. The pioneering paper of Grassl [38] brought concept of a dual lattice with aligned cracks and conduit elements allowing to accurately reflect the crack opening effect on the flow. The dual lattice approach was later extended to 3D [39]. Several other papers employ this concept, e.g., for simulation of cracking due to rebar corrosion [30] or hydraulic fracturing [68, 7, 6]. Li et al. [48] apply the dual lattice concept to shale fracture and add effects of mechanical volumetric strain rate on the pressure. Shen et al. [60] used the dual lattice concept to accurately simulate concrete thermal spalling.

Computational cost of coupled mesoscale discrete models is unfortunately still substantial and prohibits their application in design of structures and structural elements of a real size. There are several known and widely used techniques available for reducing computational complexity of numerical models. The techniques applicable for mechanical discrete mesoscale models spans from (i) coarse graining [50, 46, 1], (ii) adaptivity [25, 58, 19, 15], (iii) model order reduction such as Proper orthogonal decomposition [61, 18, 44, 13] and (iv) homogenization.

Homogenization of heterogeneous materials became a classical technique allowing major reduction of computational cost [8]. It relies on two fundamental assumptions: (i) existence of a representative volume element (RVE) or periodic unit cell, a material volume containing complete information about material internal structure and its properties; (ii) scale separation, an assumption that the size of such RVE is much smaller than the size of actual domain of the problem. For relatively simple cases, one can develop an analytical solution of the RVE response. For most cases, non-trivial constitutive equations or complex material internal structures prevent a closed-form solution. Therefore computational homogenization [62, 2, 47], sometimes called FE², has become widely employed. RVE is attached to every integration point of the macroscopic continuous homogeneous model where it serves as a “virtual experiment”. At every iteration, the RVE is appropriately loaded, a boundary value problem at microscale is numerically solved, its results are collected and returned back to the macroscale. The present paper derives a computational homogenization procedure for discrete coupled models using asymptotic expansion technique.

A fundamental challenge in computational homogenization of quasibrittle materials is strain localization. Gitman et al. [36] concluded that the assumption about the existence of RVE does not hold in presence of strain localization. Fortunately, several successful attempts were recently conducted towards solution of this problem. Kouznetsova et al. [45] extended the homogenization scheme by incorporating the second order gradients of the macroscopic displacement field to regularize the RVE problem. The same research team [17, 16] proposed a relaxed periodic boundary condition to allow formation of a crack inside the RVE under arbitrary angle. Furthermore, they separated the microscale response into a homogeneous “bulk” part and a localization related part. Similar separation of the fine scale problem into localized and homogeneous parts as well as enrichment of the RVE boundary conditions were developed by Unger [69]. The homogeneous part accounts for both elastic deformation and diffused cracking while the localized part represents regions where strain localization takes place. A mathematical basis for this extension relies on a modification of Hill–Mandel principle. Further developments of these concepts can be found in Refs. [51, 67, 65]. The strain localization problem is not addressed in this paper and is left open for further investigation.

The present paper extends work of Reza khani and Cusatis [56] who developed homogenization approach for mechanical discrete models via asymptotic expansion. The same homogenization technique is applied also in Refs. [55, 57]. Analogous strategy is taken in Ref. [29] to homogenize the mass transport problem in a discrete setup. The present paper brings a unifying technique by applying the asymptotic expansion homogenization to the coupled problem of mass transport and momentum balance [40]; the previously derived decoupled derivations appear as special cases of the coupled one developed here. The present homogenization approach is capable to provide reasonable accurate predictions at a reduced computational cost and much simpler pre-processing. Final parts of the paper demonstrate capabilities of the homogenized solution by comparing the *full* and *homogenized* models with a help of multiple examples.

2 Discrete model of the coupled problem

The asymptotic expansion homogenization developed further in this study can be generally applied to any discrete model with fixed connectivity between particles. The most prominent representant of this type of models is arguably the Lattice Discrete Particle Model (LDPM) [22, 21], which has been applied to various loading scenarios including static-like loading or highly dynamical events (e.g., projectile penetration [63, 31]). The model was originally formulated for plain and reinforced concrete but soon adapted also for short fiber reinforcement [43, 14]. It has been extended to simulate multi-physical coupled phenomena such as Alkali-Silica reaction [4, 55] or thermal spalling [60]. LDPM has been extensively validated using large sets of experiments. The wide acceptance of LDPM makes it an ideal model for the homogenization. The present paper therefore develops the homogenization for LDPM, even though a slightly modified and simplified model is used in the verification examples.

The model geometry is based on a tessellation of the computational domain into simplices (tetrahedrons in three dimensions). These tetrahedrons serve as control volumes, basic units for the mass transport problem in a fully saturated medium as the mass balance within these control volumes is preserved. The pressure degree of freedom is assigned to each of the simplices, either to its centroid or to the center of its circumscribed sphere depending on the model type. The transport nodes are hereinafter denoted P or Q (Fig. 1c). Each vertex of the simplex bears mechanical degrees of freedom (three translations and three rotations) and represents center of one mechanical rigid body/particle. For clarity, these mechanical nodes are denoted I or J (Fig. 1b). The primary variables of the coupled problem are therefore the scalar field of pressure p and vector fields of displacements \mathbf{u} and rotations $\boldsymbol{\theta}$. The compressive fluid pressure is considered to be positive.

Each transport node P at coordinates \mathbf{x}_P with pressure degree of freedom p^P is surrounded by faces (forming simplex called here the control volume) that connect it to other nodes. The connection between nodes P and Q has some area S , length $h = \|\mathbf{x}_{PQ}\|$ and contact direction $\mathbf{e}_\lambda = \mathbf{x}_{PQ}/h$, where $\mathbf{x}_{PQ} = \mathbf{x}_Q - \mathbf{x}_P$. The situation is sketched in 2D in Fig. 1c. Estimation of pressure gradient between two nodes yields

$$g = \nabla p \cdot \mathbf{e}_\lambda \approx \frac{p^Q - p^P}{h} \quad (1)$$

The transport face normal \mathbf{o} (see Fig. 1c) might not in general be parallel to the contact vector \mathbf{e}_λ . Projected area $S^* = S \mathbf{o} \cdot \mathbf{e}_\lambda$ is introduced to account for the directional mismatch when the total flux is computed later in Eq. (11).

The mechanical node I is connected to the surrounding mechanical nodes J . The contact faces form a polyhedron as shown in Fig. 1b. The strain and curvature at the contact between bodies I and J read

$$\varepsilon_\alpha = \frac{1}{l} \left(\mathbf{u}^J - \mathbf{u}^I + \boldsymbol{\varepsilon} : (\boldsymbol{\theta}^J \otimes \mathbf{c}_J - \boldsymbol{\theta}^I \otimes \mathbf{c}_I) \right) \cdot \mathbf{e}_\alpha \quad \chi_\alpha = \frac{1}{l} \left(\boldsymbol{\theta}^J - \boldsymbol{\theta}^I \right) \cdot \mathbf{e}_\alpha \quad (2)$$

where \mathbf{c} is a vector connecting particle governing node with the integration point \mathbf{x}_c at the contact face (see Fig. 1b), $\boldsymbol{\varepsilon}$ is Levi-Civita permutation symbol and \mathbf{e}_α are local normal and two tangential directions ($\alpha \in \{N, M, L\}$), respectively. The length of the contact is $l = \|\mathbf{x}_{IJ}\|$ and the contact direction $\mathbf{e}_N = \mathbf{x}_{IJ}/l$ where $\mathbf{x}_{IJ} = \mathbf{x}_J - \mathbf{x}_I$. The contact direction \mathbf{e}_N can in general be different from the true face normal \mathbf{n} . The contact area A is therefore again projected as $A^* = A \mathbf{e}_N \cdot \mathbf{n}$. Equations (1) and (2) are the compatibility equations of the model providing strain-like variables from primary fields.

The second set of equations are constitutive equations which provide stress-like variables. These are flux scalar, j , traction vector, \mathbf{t} , and couple traction vector, \mathbf{m}

$$j = f_j(p_\lambda, g, \delta_\lambda) = -\lambda(p_\lambda, \delta_\lambda)g \quad \mathbf{t} = f_s(\boldsymbol{\varepsilon}) - b p_a \mathbf{e}_N \quad \mathbf{m} = f_m(\boldsymbol{\chi}) \quad (3)$$

The first equation expresses linear dependence of the flux, j , on the pressure gradient, g , while the permeability coefficient, λ , is governed by an average normal crack opening, δ_λ , and an average pressure, p_λ , in the element. Several possible formulations are being used to describe effects of cracks [6, 7, 48] or pressure [70] on material permeability in the literature. The second constitutive equation defines another coupling between transport and mechanics as the total traction, \mathbf{t} , becomes dependent on the fluid pressure according to Biot's theory [9, 24], b is a material parameter called Biot coefficient and $\mathbf{s} = f_s(\boldsymbol{\varepsilon})$ is the vector of traction in the solid. The pressure p_a is the weighted average pressure from control volumes surrounding the mechanical element. The third constitutive equation assumes that the couple traction, \mathbf{m} , is dependent solely on the curvature, $\boldsymbol{\chi}$, i.e., decoupled from the transport part of the model. The homogenization procedure is in principle independent of the choice of the functions λ , f_s and f_m , but their dependency on other variables would require adjustments of Eqs. (38).

Finally, balance equations are assembled. The balance of linear and angular momentum of particle I read

$$V\rho\ddot{\mathbf{u}}^I + \mathbf{M}_{u\theta} \cdot \ddot{\boldsymbol{\theta}}^I - V\mathbf{b} = \sum_J A^* t_\alpha \mathbf{e}_\alpha \quad \mathbf{M}_\theta \cdot \ddot{\boldsymbol{\theta}}^I + \mathbf{M}_{u\theta}^T \cdot \ddot{\mathbf{u}}^I = \sum_J A^* [\mathbf{w} + m_\alpha \mathbf{e}_\alpha] \quad (4)$$

where $\mathbf{w} = \boldsymbol{\mathcal{E}} : (\mathbf{c}_I \otimes \mathbf{t}) = t_\alpha \boldsymbol{\mathcal{E}} : (\mathbf{c}_I \otimes \mathbf{e}_\alpha)$ is the moment of traction with respect to the mechanical node \mathbf{x}_I . \mathbf{M}_θ and $\mathbf{M}_{u\theta}$ are the moment of inertia tensors defined as

$$\mathbf{M}_\theta = \rho \int_V \mathbf{r} \cdot \mathbf{r} \mathbf{1} - \mathbf{r} \otimes \mathbf{r} dV \quad \mathbf{M}_{u\theta} = -\mathbf{M}_{u\theta}^T = \rho V \boldsymbol{\mathcal{E}} \cdot \mathbf{r}_0 \quad (5)$$

with \mathbf{r} being a vector from the particle governing node \mathbf{x}_I to any point within the particle and \mathbf{r}_0 being a vector from \mathbf{x}_I to the particle centroid; $\mathbf{1}$ is the second order identity tensor. For special case $\mathbf{r}_0 = \mathbf{0}$ when the governing node of the particle coincides with its centroid, $\mathbf{M}_{u\theta} = \mathbf{0}$. Such situation corresponds to a specific model geometry (for example the one obtained by centroidal Voronoi tessellation) but not to the general case of the described model.

Note, that the constitutive equations are computed in a rotated local reference system $[\mathbf{e}_N, \mathbf{e}_M, \mathbf{e}_L]$ and therefore both traction components need to be projected back to the \mathbf{x} reference system in the equilibrium equations. The volume of the particle is V , ρ is the solid density and \mathbf{b} represents the external load. If needed, a moment source term can be easily added to the balance of angular momentum.

The mass balance equation for a fully saturated medium is established for each control volume P separately. It is assumed that the liquid is slightly compressible with bulk modulus K_w . The pressure dependent fluid density becomes [48]

$$\rho_w = \rho_{w0} \left(1 + \frac{p_\lambda - p_0}{K_w} \right) \quad (6)$$

where p_0 is a reference pressure and ρ_{w0} is the fluid density under the reference pressure. According to the Biot's theory, we can express change of the mass of the liquid in the reference volume W as [48]

$$\rho_{w0} \left(3b\dot{\varepsilon}_{V,\text{eff}} + \frac{\dot{p}_\lambda}{M_b} \right) W \quad (7)$$

with M_b being the Biot modulus (reciprocal of capacity, c) and $\varepsilon_{V,\text{eff}}$ is the effective volumetric strain. In a discrete setup, a local volumetric strain is estimated as one third of the relative difference in a tetrahedron volume due to displacements $\varepsilon_V = [W(\mathbf{x} + \mathbf{u}) - W(\mathbf{x})]/3W(\mathbf{x})$. The effective volumetric strain is then obtained by removing the volume of cracks from the volumetric strain

$$\varepsilon_{V,\text{eff}} = \frac{W(\mathbf{x} + \mathbf{u}) - W(\mathbf{x}) - W \sum_{Q \in W} v_c}{3W(\mathbf{x})} = \varepsilon_V - \frac{1}{3} \sum_{Q \in W} v_c \quad (8)$$

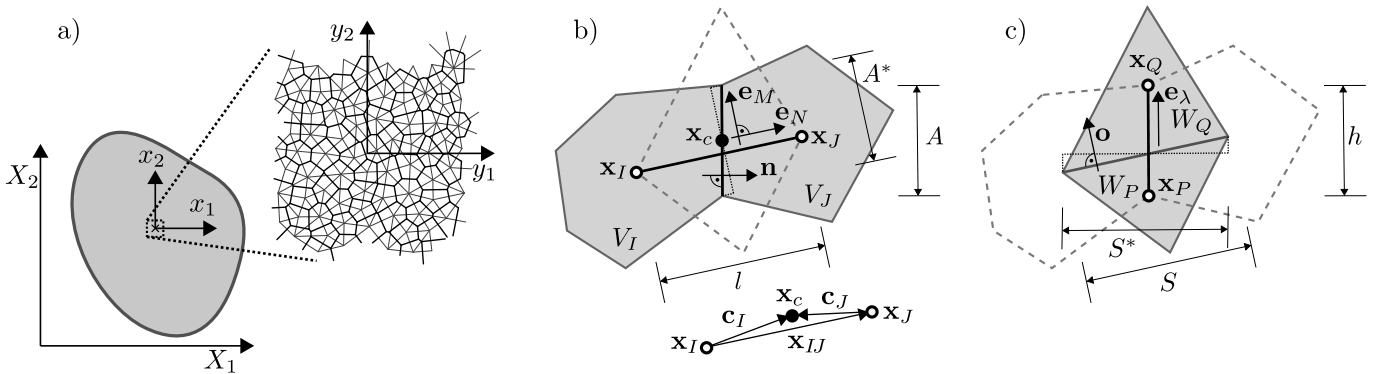


Figure 1: 2D sketch of the homogenization setup: a) different reference systems, a continuous macroscale problem and a discrete periodic microscale problem; b) a mechanical element connecting two rigid particles; c) a conduit element along the contact between two particles.

with v_c being the relative crack volume within a conduit element connecting nodes P and Q evaluated as the total crack volume in the element, V_c , divided by element volume $W_P + W_Q$. The total crack volume V_c reads

$$V_c = \sum_{\text{neighb. } e} A_f \delta_N \quad (9)$$

A_f corresponds to fractions of areas of mechanical elements, e , connected to the conduit element and δ_N are their normal openings. Finally, change of the fluid mass in time due to cracks filled with fluid becomes

$$W \frac{\partial \rho_w v_c}{\partial t} = W \left(\rho_w \dot{v}_c + v_c \rho_{w0} \frac{\dot{p}_\lambda}{K_w} \right) \quad (10)$$

Summing all the contributions together and adding also fluxes through the individual conduit elements and possible source term q (positive when material flows into the volume), the discrete mass balance equation for control volume P reads

$$\sum_{Q \in W} \left[S^* j - \rho_{w0} W \dot{v}_c \left(1 - b + \frac{p_\lambda - p_0}{K_w} \right) - \rho_{w0} W v_c \frac{\dot{p}_\lambda}{K_w} \right] - \rho_{w0} \left(3b \varepsilon_V + \frac{\dot{p}_\lambda}{M_b} \right) W - Wq = 0 \quad (11)$$

3 Separation of scales

Two spatial variables are considered now for every point in the domain: the macroscopic, slow variable \mathbf{x} and the microscopic, fast variable \mathbf{y} (see Fig. 1a). The following scale separation relationship holds

$$\mathbf{x} = \eta \mathbf{y} \quad (12)$$

with η being the separation of scales constant with properties $0 < \eta \ll 1$. The model appears continuous from the viewpoint of reference system \mathbf{x} but discrete in the reference system \mathbf{y} for sufficiently small η .

Moreover, another global reference system \mathbf{X} that uniquely defines position in the continuous macroscopic space is introduced. System \mathbf{X} has the same units as \mathbf{x} but there is only one such system while infinitely many \mathbf{x} reference systems are defined in all macroscopic spatial points.

All the variables involving length are considered to be in the \mathbf{x} reference system. One needs to transfer them into the \mathbf{y} reference system according to the following transformation rules (the powers of η reflect the power of the distance unit involved, $\tilde{\bullet}$ denotes variable \bullet in \mathbf{y} reference system)

$$\begin{aligned} \mathbf{x}_{IJ} &= \eta \mathbf{y}_{IJ} & l &= \eta \tilde{l} & A^* &= \eta^2 \tilde{A}^* & V &= \eta^3 \tilde{V} & \mathbf{M}_{u\theta} &= \eta^4 \tilde{\mathbf{M}}_{u\theta} & \mathbf{M}_\theta &= \eta^5 \tilde{\mathbf{M}}_\theta \\ \mathbf{x}_{PQ} &= \eta \mathbf{y}_{PQ} & h &= \eta \tilde{h} & S^* &= \eta^2 \tilde{S}^* & W &= \eta^3 \tilde{W} & \mathbf{c}_J &= \eta \tilde{\mathbf{c}}_J \end{aligned} \quad (13)$$

The primary variables p , \mathbf{u} and $\boldsymbol{\theta}$ are now considered to be approximated by several components, especially by the macroscopic component, $\bullet^{(0)}$, and the microscopic component, $\bullet^{(1)}$. Expansion of the pressure and displacements is straightforward. Expansion of rotations is done according to Reza khani and Cusatis [56] by assuming existence of some continuous displacement-like field \mathbf{d} the curl of which provides the rotations: $2\boldsymbol{\theta} = \nabla \times \mathbf{d}$. The expansion of the rotations is taken as curls of the expanded field \mathbf{d} with nabla operator transferred in accordance with Eq. (12) into $\nabla = \nabla_X + \eta^{-1} \nabla_y$. The three asymptotic expansion equations read

$$p(\mathbf{X}, \mathbf{y}) = \eta^{-1} p^{(-1)}(\mathbf{X}, \mathbf{y}) + p^{(0)}(\mathbf{X}, \mathbf{y}) + \eta p^{(1)}(\mathbf{X}, \mathbf{y}) + \dots \quad (14a)$$

$$\mathbf{u}(\mathbf{X}, \mathbf{y}) = \mathbf{u}^{(0)}(\mathbf{X}, \mathbf{y}) + \eta \mathbf{u}^{(1)}(\mathbf{X}, \mathbf{y}) + \dots \quad (14b)$$

$$\boldsymbol{\theta}(\mathbf{X}, \mathbf{y}) = \eta^{-1} \boldsymbol{\omega}^{(-1)}(\mathbf{X}, \mathbf{y}) + \boldsymbol{\omega}^{(0)}(\mathbf{X}, \mathbf{y}) + \boldsymbol{\varphi}^{(0)}(\mathbf{X}, \mathbf{y}) + \eta \boldsymbol{\varphi}^{(1)}(\mathbf{X}, \mathbf{y}) + \dots \quad (14c)$$

where $2\boldsymbol{\omega}^{(-1)} = \nabla_y \times \mathbf{d}^{(0)}$, $2\boldsymbol{\omega}^{(0)} = \nabla_y \times \mathbf{d}^{(1)}$, $2\boldsymbol{\varphi}^{(0)} = \nabla_X \times \mathbf{d}^{(0)}$ and $2\boldsymbol{\varphi}^{(1)} = \nabla_X \times \mathbf{d}^{(1)}$. Note that the expansion of pressure should correspond to the expansion of the traction in mechanical models (Eq. 19b). Therefore, term $\eta^{-1} p^{(-1)}$ is included as well. All of the fields are assumed to be y -periodic over some Representative Volume Element (RVE) with periodic geometrical structure of the discrete model. It is also assumed that all these fast fields (or fluctuations) yield zero average over the RVE.

From the viewpoint of the macroscopic spatial coordinate \mathbf{X} , neighboring mechanical nodes I and J are close to each other. According to Fish et al. [32], one can use the macroscopic gradient $\nabla_{\mathbf{X}}$ at node I to approximate the mechanical field variables at node J . The same Taylor expansion of pressure around node P provides pressure estimation at neighboring node Q .

$$p(\mathbf{X}_Q, \mathbf{y}_Q) = p(\mathbf{X}_P, \mathbf{y}_Q) + \frac{\partial p(\mathbf{X}_P, \mathbf{y}_Q)}{\partial X_i} x_i^{PQ} + \frac{1}{2} \frac{\partial^2 p(\mathbf{X}_P, \mathbf{y}_Q)}{\partial X_i \partial X_j} x_i^{PQ} x_j^{PQ} + \dots \quad (15a)$$

$$\mathbf{u}(\mathbf{X}_J, \mathbf{y}_J) = \mathbf{u}(\mathbf{X}_I, \mathbf{y}_J) + \frac{\partial \mathbf{u}(\mathbf{X}_I, \mathbf{y}_J)}{\partial X_j} x_j^{IJ} + \frac{1}{2} \frac{\partial^2 \mathbf{u}(\mathbf{X}_I, \mathbf{y}_J)}{\partial X_j \partial X_k} x_j^{IJ} x_k^{IJ} + \dots \quad (15b)$$

$$\boldsymbol{\theta}(\mathbf{X}_J, \mathbf{y}_J) = \boldsymbol{\theta}(\mathbf{X}_I, \mathbf{y}_J) + \frac{\partial \boldsymbol{\theta}(\mathbf{X}_I, \mathbf{y}_J)}{\partial X_j} x_j^{IJ} + \frac{1}{2} \frac{\partial^2 \boldsymbol{\theta}(\mathbf{X}_I, \mathbf{y}_J)}{\partial X_j \partial X_k} x_j^{IJ} x_k^{IJ} + \dots \quad (15c)$$

The compatibility equations (1) and (2) are now rewritten

$$g = \frac{1}{h} [p(\mathbf{X}_Q, \mathbf{y}_Q) - p(\mathbf{X}_P, \mathbf{y}_P)] \quad (16a)$$

$$\varepsilon_\alpha = \frac{1}{l} [\mathbf{u}(\mathbf{X}_J, \mathbf{y}_J) - \mathbf{u}(\mathbf{X}_I, \mathbf{y}_I) + \boldsymbol{\varepsilon} : (\boldsymbol{\theta}(\mathbf{X}_J, \mathbf{y}_J) \otimes \mathbf{c}_J - \boldsymbol{\theta}(\mathbf{X}_I, \mathbf{y}_I) \otimes \mathbf{c}_I)] \cdot \mathbf{e}_\alpha \quad (16b)$$

$$\chi_\alpha = \frac{1}{l} [\boldsymbol{\theta}(\mathbf{X}_J, \mathbf{y}_J) - \boldsymbol{\theta}(\mathbf{X}_I, \mathbf{y}_I)] \cdot \mathbf{e}_\alpha \quad (16c)$$

and the Taylor expansion (15) as well as the asymptotic expansion (14) is substituted afterwards. Note that thanks to the Taylor expansion, there is always the same \mathbf{X} coordinate (either \mathbf{X}_P or \mathbf{X}_I) denoting the RVE location. The equations must hold for any \mathbf{X} coordinate (or any RVE), therefore we can drop it for sake of simplicity. As long as only a single RVE is involved (constant \mathbf{X} coordinate) the notation can be simplified $\bullet^{\alpha P} = \bullet^{(\alpha)}(\mathbf{X}, \mathbf{y}_P)$. For example, \mathbf{u}^{0I} means $\mathbf{u}^{(0)}(\mathbf{X}, \mathbf{y}_I)$ hereinafter.

The set of compatibility equations (16) with substituted (14) and (15) and scaled length variables (13) reads

$$g = \eta^{-2} g^{(-2)} + \eta^{-1} g^{(-1)} + g^{(0)} + \eta g^{(1)} + \dots \quad (17a)$$

$$\varepsilon_\alpha = \eta^{-1} \varepsilon_\alpha^{(-1)} + \varepsilon_\alpha^{(0)} + \eta \varepsilon_\alpha^{(1)} + \dots \quad (17b)$$

$$\chi_\alpha = \eta^{-2} \chi_\alpha^{(-2)} + \eta^{-1} \chi_\alpha^{(-1)} + \chi_\alpha^{(0)} + \dots \quad (17c)$$

The individual components can be found in Eqs. (37) in Appendix A.

Next, the volumetric strain, ε_V , crack opening, δ_N , and cracks volume density, v_c , are expanded. Volumetric strain, defined as one third of the relative change of the volume of the tetrahedron, is directly dependent on displacements \mathbf{u} according to Eq. (8). Since it is a strain variable, its expansion must be the same as expansion of the strain. Normal crack opening δ_N is dependent on strain ε_N by subtracting its elastic part and multiplying the result by length l . The relative crack volume v_c is dependent on crack opening δ_N by multiplying it by the crack area A_f and divided by the element volume. The expansions therefore read

$$\varepsilon_V = \eta^{-1} \varepsilon_V^{(-1)} + \varepsilon_V^{(0)} + \eta \varepsilon_V^{(1)} + \dots \quad (18a)$$

$$\delta_N = \delta_N^{(0)} + \eta \delta_N^{(1)} + \eta^2 \delta_N^{(2)} + \dots \quad (18b)$$

$$v_c = \eta^{-1} v_c^{(-1)} + v_c^{(0)} + \eta v_c^{(1)} + \dots \quad (18c)$$

The stress-like variables (flux, traction, couple traction and moment of traction) are also expanded into

$$j = \eta^{-2} j^{(-2)} + \eta^{-1} j^{(-1)} + j^{(0)} + \eta j^{(1)} + \dots \quad (19a)$$

$$\mathbf{t} = \eta^{-1} \mathbf{t}^{(-1)} + \mathbf{t}^{(0)} + \eta \mathbf{t}^{(1)} + \dots \quad (19b)$$

$$\mathbf{m} = \mathbf{m}^{(0)} + \eta \mathbf{m}^{(1)} + \eta^2 \mathbf{m}^{(2)} + \dots \quad (19c)$$

$$\mathbf{w} = \mathbf{w}^{(0)} + \eta \mathbf{w}^{(1)} + \eta^2 \mathbf{w}^{(2)} + \dots \quad (19d)$$

It will be shown in Secs. 4.1 and 4.2 that terms $j^{(-2)}$, $j^{(-1)}$, $\mathbf{t}^{(-1)}$, $\mathbf{m}^{(0)}$, $\mathbf{w}^{(0)}$ as well as $g^{(-2)}$, $g^{(-1)}$, $\varepsilon^{(-1)}$, $\boldsymbol{\chi}^{(-2)}$, $\delta_\lambda^{(0)}$ and $p^{(-1)}$ are always zero. Therefore the first nonzero terms in expansion (19) are expressed by components of the

constitutive relations (3) with the lowest η powers

$$j^{(0)} = -\lambda \left(p_\lambda^{(0)}, \eta \delta_\lambda^{(1)} \right) g^{(0)} \quad (20a)$$

$$\mathbf{t}^{(0)} = f_s \left(\boldsymbol{\varepsilon}^{(0)} \right) - p_a^{(0)} b \mathbf{e}_N \quad (20b)$$

$$\eta \mathbf{m}^{(1)} = f_m \left(\eta^{-1} \boldsymbol{\chi}^{(-1)} \right) \quad (20c)$$

$$\eta \mathbf{w}^{(1)} = t_\alpha^{(0)} \boldsymbol{\varepsilon} : (\mathbf{c}_I \otimes \mathbf{e}_\alpha) \quad (20d)$$

These equations represent the actual constitutive equations of the discrete model. The second nonzero components of stress-like variables are developed via Taylor series in Eqs. (38) in Appendix B.

The source terms q and \mathbf{b} (as well as other variables, e.g. Biot coefficient b , capacity c or density ρ) might also be dependent on the primary or other fields. For example recent study [53] suggests that damage dependent Biot coefficient should be used for hydraulic fracturing simulations. In such cases, their expansion must be developed as well and added to the balance equations in the next section. It is assumed here, for sake of simplicity, that these variables are independent on the primary fields and have only one component of order $\approx \mathcal{O}(\eta^0)$. Reader interested in the described extension is referred to paper [29] where such expansion is developed for q and c .

4 Balance equations

The balance equations of individual particles or control volumes are now assembled in the \mathbf{x} reference system using variables transformed into the \mathbf{y} reference system. Starting with Eqs. (4) and (11), assuming all material parameters are of order $\approx \mathcal{O}(\eta^0)$, transforming all the length variables from \mathbf{x} to \mathbf{y} reference system, and dividing everything by η^3 , η^3 or η^4 , respectively, the balance equations read

$$\rho_{w0} \tilde{W} \left(3b \dot{\varepsilon}_V + \frac{\dot{p}_\lambda}{M_b} \right) + \tilde{W} q = \frac{1}{\eta} \sum_{Q \in W} \left[\tilde{S}^* j - \eta \rho_{w0} \tilde{W} \dot{v}_c \left(1 - b + \frac{p_\lambda - p_0}{K_w} \right) - \eta \rho_{w0} \tilde{W} v_c \frac{\dot{p}_\lambda}{K_w} \right] \quad (21a)$$

$$\tilde{V} \rho \ddot{\mathbf{u}}^I + \eta \tilde{\mathbf{M}}_{u\theta} \cdot \ddot{\boldsymbol{\theta}}^I - \tilde{V} \mathbf{b} = \frac{1}{\eta} \sum_J \tilde{A}^* t_\alpha \quad (21b)$$

$$\eta \tilde{\mathbf{M}}_\theta \cdot \ddot{\boldsymbol{\theta}}^I + \tilde{\mathbf{M}}_{u\theta}^T \cdot \ddot{\mathbf{u}}^I = \frac{1}{\eta^2} \sum_J \tilde{A}^* (\mathbf{w} + m_\alpha \mathbf{e}_\alpha) \quad (21c)$$

The expansions developed in Eqs. (14), (17), (18) and (19) can now be substituted into the balance equations, which can be then decomposed into separate equation sets collecting the terms with corresponding powers of η .

4.1 η^{-3} : zero pressure $\eta^{-1} p^{(-1)}$

The expansion of pressure involves the term $\eta^{-1} p^{(-1)}$, which gives rise to pressure gradient $\eta^{-2} g^{(-2)}$ and flux $\eta^{-2} j^{(-2)}$. The balance equation (21a) then contains term with η^{-3} which, when brought back to the \mathbf{x} reference system and multiplied by η^3 , reads

$$\eta^{-2} \sum_{Q \in W} S^* j^{(-2)} = 0 \quad (22)$$

Equation (22) must be satisfied for all control volumes and periodicity in the y reference system must be obeyed. An obvious solution and also the only possible one in the case of a linear behavior is constant pressure $\eta^{-1} p^{-1}$ over the whole RVE resulting in zero pressure gradient and flux $\eta^{-2} g^{(-2)} = \eta^{-2} j^{(-2)} = 0$. Since the pressure term with the lowest η power prescribed by boundary conditions is $p^{(0)}$, the pressure $\eta^{-1} p^{(-1)} = 0$ everywhere. There might exist other solutions to Eq. (22) in the nonlinear regime of the constitutive relation but one can reasonably assume that the trivial solution is always the correct one.

4.2 η^{-2} : constantness of macroscopic fields over RVE

Terms with the negative second power of η brought back to the \mathbf{x} reference system and multiplied by η^3 , η^3 and η^4 , respectively, yield

$$\eta^{-1} \sum_{Q \in W} S^* j^{(-1)} = 0 \quad (23a)$$

$$\eta^{-1} \sum_{J \in V} A^* t_\alpha^{(-1)} \mathbf{e}_\alpha = \mathbf{0} \quad (23b)$$

$$\sum_{J \in V} A^* \left(\mathbf{w}^{(0)} + m_\alpha^{(0)} \mathbf{e}_\alpha \right) = \mathbf{0} \quad (23c)$$

Assembling these three equations for all particles and control volumes inside the RVE and considering the periodic boundary conditions, we obtain system with degrees of freedom $p^{(0)}$, $\mathbf{u}^{(0)}$ and $\eta^{-1} \boldsymbol{\omega}^{(-1)}$. Let us again consider linearity of the constitutive model. The solution must then be constant pressure $p^{(0)}$ and rigid body motion of the whole RVE defined as $\mathbf{u}^{(0)} = \mathbf{v}^{(0)} + \eta^{-1} \boldsymbol{\varepsilon} : (\boldsymbol{\omega}^{(-1)} \otimes \mathbf{x})$ providing zero corresponding strain- and stress-like variables as listed bellow Eq. (19). Moreover, the volumetric strain $\varepsilon_V^{(-1)}$, normal crack openings $\delta_N^{(0)}$ and $\delta_\lambda^{(0)}$ and relative crack volume $v_c^{(-1)}$ are zero as well because they depend on the strain $\boldsymbol{\varepsilon}^{(-1)}$. Contrarily to what was done in Ref. [56], the solutions of Eqs. 23 must be periodic in the y coordinate, and therefore one must conclude that $\boldsymbol{\omega}^{(-1)} = \mathbf{0}$. This renders the displacement $\mathbf{u}^{(0)}$ constant over the RVE. This is the same result one obtains at the same length scale and using the periodicity assumption in the classical mathematical homogenization [33, 35].

Similarly to the previous scale, other solutions might exist in the nonlinear regime, but the presented trivial solution to system (23) will always be assumed to be the only correct one. The variables $p^{(0)}$ and $\mathbf{u}^{(0)}$ remain unknown. They represent constant macroscopic pressure over the RVE and the RVE macroscopic translation. Thanks to the constantness of $p^{(0)}$, one may replace the averages of the pressure by a constant hereinafter: $p_\lambda^{(0)} = p_a^{(0)} = p^{(0)}$.

4.3 η^{-1} : RVE problem

The negative first power of η collects the following terms (already transformed to \mathbf{x} reference system and multiplied by η^3 , η^3 and η^4 , respectively)

$$\sum_{Q \in W} S^* j^{(0)} = 0 \quad (24a)$$

$$\sum_{J \in V} A^* s_\alpha^{(0)} \mathbf{e}_\alpha = p^{(0)} \sum_{J \in V} A^* b \mathbf{e}_N \quad (24b)$$

$$\sum_{J \in V} A^* \left(s_\alpha^{(0)} \mathbf{e}_\alpha \boldsymbol{\varepsilon} : (\mathbf{c}_I \otimes \mathbf{e}_N) + \eta m_\alpha^{(1)} \mathbf{e}_\alpha \right) = p^{(0)} \boldsymbol{\varepsilon} : \sum_{J \in V} A^* b \mathbf{c}_I \otimes \mathbf{e}_N \quad (24c)$$

Note that terms containing $v_c^{(-1)}$ and $\varepsilon_V^{(-1)}$ are already removed from the flux balance equation because these variables are zero. Also, traction $\mathbf{t}^{(0)}$ and moment of traction $\eta \mathbf{w}^{(1)}$ are replaced according to their definitions from Eqs. (20b) and (20d), $\mathbf{s}^{(0)} = f_s(\boldsymbol{\varepsilon}^{(0)})$ is the traction in the solid.

The pressure gradients, strains and curvatures that give rise to fluxes, tractions, couple tractions and moments of tractions are $g^{(0)}$, $\boldsymbol{\varepsilon}^{(0)}$ and $\eta^{-1} \boldsymbol{\chi}^{(-1)}$ defined by Eqs. (37c), (37f) and (37i). These equations are rewritten based on the previous solution at η^{-2} and η^{-3} scale ($\eta^{-1} p^{(-1)} = 0$, $\eta^{-1} \boldsymbol{\omega}^{(-1)} = \mathbf{0}$, $\mathbf{u}^{(0)}$ and $p^{(0)}$ are constant) and using identity $\mathbf{y}_{IJ} = \tilde{\mathbf{c}}_I - \tilde{\mathbf{c}}_J$ (Fig. 1b)

$$g^{(0)} = \frac{\eta}{h} [p^{1Q} - p^{1P}] - \hat{g} \quad (25a)$$

$$\varepsilon_\alpha^{(0)} = \frac{e_i^\alpha}{l} [\eta u_i^{1J} - \eta u_i^{1I} + \mathcal{E}_{ijk} \omega_j^{0J} c_k^J - \mathcal{E}_{ijk} \omega_j^{0I} c_k^I] - \hat{\varepsilon}_\alpha \quad (25b)$$

$$\eta^{-1} \chi_\alpha^{(-1)} = \frac{e_i^\alpha}{l} [\omega_i^{0J} - \omega_i^{0I}] \quad (25c)$$

where eigen-pressure gradient \hat{g} and eigen-strain $\hat{\epsilon}_\alpha$ turn out to be negative projections of the macroscopic pressure gradient $\mathbf{a} = \nabla_X p^{(0)}$ and the Cosserat strain tensor $\boldsymbol{\gamma} = \nabla_X \otimes \mathbf{u}^{(0)} - \boldsymbol{\mathcal{E}} \cdot \boldsymbol{\varphi}^{(0)}$

$$\hat{g} = -\frac{\partial p^{(0)}}{\partial X_i} e_i^\lambda = -\mathbf{a} \cdot \mathbf{e}_\lambda \quad (26a)$$

$$\hat{\epsilon}_\alpha = -e_i^\alpha \left[\frac{\partial u_i^{(0)}}{\partial X_k} - \mathcal{E}_{ijk} \varphi_j^{(0)} \right] e_k^N = -\mathbf{e}_N \cdot \boldsymbol{\gamma} \cdot \mathbf{e}_\alpha \quad (26b)$$

Both vector \mathbf{a} and tensor $\boldsymbol{\gamma}$ are provided by the macroscopic problem to be described later. Vector $\boldsymbol{\varphi}^{(0)}$ shall be identified from its definition as a macroscopic rotation of the RVE and therefore is constant over the RVE. The projection of the macroscopic Cosserat curvature that was derived in Ref. [56] is missing here because in the current derivation $\boldsymbol{\omega}^{(-1)} = \mathbf{0}$.

All three balance equations (24) to be solved numerically are steady state (or static) equations; the transient terms are not present. Unknown fields in these problems are $\eta p^{(1)}$, $\eta \mathbf{u}^{(1)}$ and $\boldsymbol{\omega}^{(0)}$ being the microscopic pressure, translation and rotation, respectively. Note that these problems are partially decoupled. The mechanical RVE depends only on the macroscopic pressure $p^{(0)}$, primary field $\eta p^{(1)}$ has no effect on the mechanical behavior. The transport problem, however, depends on mechanical primary field $\eta \mathbf{u}^{(1)}$ via the crack opening $\eta \delta_N^{(1)}$. One should therefore first solve the mechanical RVE problem and then use the computed crack openings $\eta \delta_N^{(1)}$ when solving the transport RVE problem.

The transport RVE is loaded only by the projection of the macroscopic pressure gradient in the form of eigen-pressure gradient. The load applied to the mechanical RVE comes from the macroscale in two ways: (i) in the form of eigen-strain and (ii) as a force and moment acting on each particle due to the macroscopic fluid pressure as the right-hand side terms in Eqs. (24).

The periodic boundary conditions must be enforced for pressure, displacements and rotations. Furthermore, equations (25) consider only differences in the primary fields of displacements and pressure and are ill-conditioned without an additional constraint. The assumption behind the asymptotic expansion (14) requires the microscopic fields (fluctuations) to be zero on average, therefore the last boundary conditions should prescribe zero volumetric average of these fields over the RVE

$$\langle \eta p^{(1)} \rangle = 0 \quad \langle \eta \mathbf{u}^{(1)} \rangle = \mathbf{0} \quad (27)$$

where the weighted volumetric average reads

$$\langle \bullet \rangle = \frac{1}{V_0} \sum_{w \in V_0} V_w \bullet \quad (28)$$

with V_w being volume (V_I or W_P) associated with the mechanical or mass transport node and w denotes either mechanical (e) or conduit (d) elements.

Direct enforcement of boundary conditions (27) is not practical. If one applies the linear constraint, the system matrix becomes full and computational and storage requirements rapidly grow. It is therefore recommended to randomly pick some node where pressure and translations are directly prescribed to be some random values (the easiest is to set everything to zero). After the solution is found, both pressure and displacement fast fields can be shifted to satisfy the required constraint, i.e., equations (27) are enforced during the post-processing. Moreover, the actual fast primary fields are typically not required and one can skip this post-processing step.

4.4 η^0 : macroscopic level

Terms with zero power of η , already transformed to \mathbf{x} reference system and multiplied by η^3 , η^3 and η^4 , respectively, are the following (note that terms with $v_c^{(1)}$ and $\boldsymbol{\omega}^{(-1)}$, which are always zero, are already deleted)

$$\sum_{Q \in W} \left[\eta S^* j^{(1)} - \rho_{w0} W v_c^{(0)} \left(1 - b + \frac{p^{(0)} - p_0}{K_w} \right) - \rho_{w0} W v_c^{(0)} \frac{\dot{p}^{(0)}}{K_w} \right] = \rho_{w0} \left(3b \hat{\epsilon}_V^{(0)} + \frac{\dot{p}^{(0)}}{M_b} \right) W + W q \quad (29a)$$

$$\eta \sum_{J \in V} A^* t_\alpha^{(1)} = V \rho \ddot{\mathbf{u}}^{(0)} - V \mathbf{b} \quad (29b)$$

$$\eta^2 \sum_{J \in V} A^* \left(\mathbf{w}^{(2)} + m_\alpha^{(2)} \mathbf{e}_\alpha \right) = \mathbf{M}_{u\theta}^T \cdot \ddot{\mathbf{u}}^{(0)} \quad (29c)$$

The balance of the whole RVE unit is of interest at the macrolevel, therefore equations for all the bodies within the RVE are summed and divided by the RVE volume, V_0 . One arrives, after several mathematical modifications reported in detail in Appendix C, to partial differential equations describing balance of mass and linear and angular momentum. The momentum balance equations correspond to Cosserat (micromorphic) continuum coupled with mass transport via Biot's theory and cracking

$$\nabla_X \cdot \mathbf{f} = \rho_{w0} \left[\dot{v}_{c0} \left(1 - b + \frac{p^{(0)} - p_0}{K_w} \right) + v_{c0} \frac{\dot{p}^{(0)}}{K_w} + 3b\dot{\varepsilon}_V^{(0)} + \frac{\dot{p}^{(0)}}{M_b} \right] + q \quad (30a)$$

$$\nabla_X \cdot \boldsymbol{\sigma}_s - \nabla_X p^{(0)} \cdot \boldsymbol{\xi} = \langle \rho \rangle \ddot{\mathbf{u}}^{(0)} - \mathbf{b} \quad (30b)$$

$$\nabla_X \cdot \boldsymbol{\mu}_s - \nabla_X p^{(0)} \cdot \boldsymbol{\zeta} + \boldsymbol{\mathcal{E}} : \boldsymbol{\sigma}_s - p^{(0)} \boldsymbol{\mathcal{E}} : \boldsymbol{\xi} = \mathbf{0} \quad (30c)$$

with the following macroscopic tensors transforming information from the RVE to the macroscale

$$\mathbf{f} = \frac{1}{V_0} \sum_{d \in V_0} h S^* j^{(0)} \mathbf{e}_\lambda \quad (31a)$$

$$\boldsymbol{\sigma}_s = \frac{1}{V_0} \sum_{e \in V_0} l A^* s_\alpha^{(0)} \mathbf{e}_N \otimes \mathbf{e}_\alpha \quad (31b)$$

$$\boldsymbol{\mu}_s = \frac{1}{V_0} \sum_{e \in V_0} l A^* \mathbf{e}_N \otimes \left[\eta m_\alpha^{(1)} \mathbf{e}_\alpha + s_\alpha^{(0)} \boldsymbol{\mathcal{E}} : (\mathbf{x}_c \otimes \mathbf{e}_\alpha) \right] \quad (31c)$$

$$\boldsymbol{\xi} = \frac{1}{V_0} \sum_{e \in V_0} l A^* b \mathbf{e}_N \otimes \mathbf{e}_N \quad (31d)$$

$$\boldsymbol{\zeta} = \frac{1}{V_0} \sum_{e \in V_0} l A^* b \mathbf{e}_N \otimes [\boldsymbol{\mathcal{E}} : (\mathbf{x}_c \otimes \mathbf{e}_N)] \quad (31e)$$

\mathbf{f} is the flux vector, $\boldsymbol{\sigma}_s$ is the solid stress tensor, $\boldsymbol{\mu}_s$ is the solid couple stress tensor and $\boldsymbol{\xi}$ and $\boldsymbol{\zeta}$ are second order tensors describing RVE internal structure producing an effect of pressure on the macroscopic stress and couple stress. As the RVE geometry remains unchanged during the calculation, $\boldsymbol{\xi}$ and $\boldsymbol{\zeta}$ are constant tensors evaluated only once at the simulation initiation. Evaluation of volumetric strain $\varepsilon_V^{(0)}$ used in Eq. (30a) is derived in Appendix D.

The primary fields (unknowns) at the macroscale are pressures $p^{(0)}$, displacements $\mathbf{u}^{(0)}$ and rotations $\boldsymbol{\varphi}^{(0)}$. Several emerging coupling terms are obtained describing storage of the fluid in cracks and an effect of volumetric changes on the pressure (Eq. 30a), an effect of the pressure gradient on the linear momentum balance (Eq. 30b), and effects of the pressure gradient and the pressure on the angular momentum balance (Eq. 30c). The macroscopic equations are naturally anisotropic due to the heterogeneity and cracking at the microscale.

The macroscale problem shall be supplemented with appropriate boundary conditions and solved, e.g., by finite element method. At each integration point, the macroscopic pressure gradient \mathbf{a} and the Cosserat strain tensor $\boldsymbol{\gamma}$ are computed and projected onto the RVE problem (Eqs. 26) from which stress-like variables (Eqs. 31) are evaluated. According to Ref. [56] the Cosserat effect does not contribute in a significant way and simplification to Cauchy continuum is possible. Also note that no transient term appears in the balance of angular momentum (30c) at this scale.

5 Parallel normal and contact vectors

The equations can be further simplified under two assumptions: (i) the Biot coefficient b is constant within the RVE and (ii) the normal and contact vectors are parallel, $\mathbf{e}_N \parallel \mathbf{n}$. The first assumption is satisfied when an identical material is used in the whole RVE domain and allows to move Biot coefficient in front of the summations. The second assumption holds when model geometry is based on Voronoi or power/Laguerre tessellation and ensures that $A^* = A$.

Let us first derive two useful identities from the divergence theorem. When the area multiplied by outward normal is summed over enclosed surface Γ , the following holds

$$\sum_{J \in V} A \mathbf{e}_N = \int_{\Gamma} e_i^N d\Gamma = \int_{\Gamma} \mathbf{i} \cdot \mathbf{e}_N d\Gamma = \int_V \nabla \cdot \mathbf{i} dV = \mathbf{0} \quad (32)$$

The second identity sums multiplication of area, its centroid and outward normal over enclosed surface of some discrete body around node I

$$\sum_{J \in V} A \mathbf{c}_I \otimes \mathbf{e}_N = \int_{\Gamma} \mathbf{r} \otimes \mathbf{e}_N d\Gamma = \int_{\Gamma} r_i e_j^N d\Gamma = \int_{\Gamma} r_i \mathbf{j} \cdot \mathbf{e}_N d\Gamma = \int_V \nabla \cdot (r_i \mathbf{j}) dV = \int_V \frac{\partial r_i}{\partial X_j} dV = \int_V \delta_{ij} dV = \mathbf{1}V \quad (33)$$

The vector \mathbf{r} serves as a general position vector pointing from node \mathbf{x}_I to any point on the particle surface or in its volume, \mathbf{i} and \mathbf{j} are unit Cartesian basis vectors and $\mathbf{1} = \delta_{ij}$ is the second order identity tensor (Kronecker delta).

Let us first show that right-hand sides of Eqs. (24b) and (24c) disappear. Simple application of identities (32) and (33) provides

$$p^{(0)} b \sum_{J \in V} A \mathbf{e}_N = 0 \quad (34a)$$

$$p^{(0)} b \boldsymbol{\varepsilon} : \sum_{J \in V} A \mathbf{c}_I \otimes \mathbf{e}_N = p^{(0)} b V \boldsymbol{\varepsilon} : \mathbf{1} = \mathbf{0} \quad (34b)$$

Therefore, constant Biot coefficient and parallelism $\mathbf{e}_N \parallel \mathbf{n}$ make the mechanical RVE problem completely independent of the pressure.

Moreover, tensor $\boldsymbol{\xi}$ from Eq. (31d) can be simplified. Recalling $l \mathbf{e}_N = \mathbf{x}^{IJ} = \mathbf{c}_I - \mathbf{c}_J$, the summations can be rewritten from summing over mechanical elements to double summations over rigid bodies and then over all its neighbors

$$\boldsymbol{\xi} = \frac{b}{V_0} \sum_{e \in V_0} A (\mathbf{c}_I - \mathbf{c}_J) \otimes \mathbf{e}_N = \frac{b}{V_0} \sum_{I \in V_0} \sum_{J \in V} A \mathbf{c}_I \otimes \mathbf{e}_N = \frac{b}{V_0} \sum_{I \in V_0} V \mathbf{1} = b \mathbf{1} \quad (35)$$

Therefore, in Eq. (30c), the term with $\boldsymbol{\xi}$ cancels out as $\boldsymbol{\varepsilon} : \mathbf{1} = \mathbf{0}$.

Finally, let us also comment on tensor $\boldsymbol{\zeta}$. The assumption of constant Biot coefficient b and parallel normal and contact vector does not simplify it. This tensor provides, when multiplied by pressure gradient, overall moment density due to the pressure gradient. It would be zero only for very specific case of no eccentricities – when all vectors \mathbf{c}_I and \mathbf{c}_J are scalar multiple of corresponding normal vector \mathbf{e}_N . This implies that the governing nodes bearing degrees of freedom are located at centroids of the rigid bodies. The described situation is theoretically achievable for some regular arrangements or when using centroidal Voronoi tessellation. However, both of these cases introduce large directional bias into the model and are of no practical use.

6 Implementation

The *full* and *homogenized* models are implemented in an in-house software. Both steady state and transient simulations are presented in the following text, however, the transient terms are only used for the mass transport part; mechanical behavior is always quasi-static in the following verification studies. Implicit time integration scheme called the generalized- α method with spectral radius 0.8 is adopted [12, 42]; the two-way coupled problem of mechanical equilibrium and transport is solved in a strongly coupled numerical scheme ensuring second order accuracy.

The mechanical constitutive model (function f_s from Eq. 3) is a simplified older version of the Lattice-Discrete Particle Model (LDPM) according to Ref. [20]. The simplification consists mostly in reducing the number of material parameters to 4 and omitting the confinement effect. Nevertheless, the full LDPM constitutive model can be easily used in the homogenization. The function f_m from Eq. (3) relating curvature and couple traction at the contact face is assumed zero. The transport constitutive relation (function f_j from Eq. 3) is a simple linear dependency of flux on the pressure gradient in intact material with additional terms according to Ref. [39] when cracks are present. The nonlinear behavior in uncracked material can also be easily homogenized as is done in Ref. [29]. Both mechanical and transport constitutive formulations are described in detail in Appendix E, which includes values of all the material model parameters listed in Tab. 1.

The spatial discretization is based on an actual mesostructure, it shall be called *physical* according to Ref. [11]. Radii of the spherical particles are obtained from the Fuller curve [34]. The location of the particles in the domain is generated randomly in a sequence restricting overlapping. The power/Laguerre tessellation provides transport connectivity and

the discrete bodies for mechanics while (weighted) Delaunay triangulation gives mechanical connectivity and control volumes for the transport part. Such discretization ensures parallelism of normal and contact vectors: $\mathbf{o} \parallel \mathbf{e}_\lambda$ and $\mathbf{e}_N \parallel \mathbf{n}$, therefore $S \equiv S^*$ and $A \equiv A^*$. Since Biot coefficient is kept spatially constant, the simplifications described in Sec. 5 hold. All the verification examples assume material with maximum aggregate diameter $d_{\max} = 10$ mm and aggregate relative volumetric content 80%. For sake of computational feasibility, only aggregates with diameter above 4 mm are explicitly considered, the rest is phenomenologically represented by the contact constitutive behavior.

Rezakhani and Cusatis [56] showed that cubic RVE with edge length $5d_{\max}$ is already sufficient for the mechanical problem. According to Ref. [29], such RVE size is acceptable also for the transport problem. Therefore, the RVE used here for all the calculation has size $50 \times 50 \times 50$ mm³; the mechanical RVE has 1,539 degrees of freedom (DoF) and the transport RVE has 2,160 DoF. A nonlinear steady-state solver is used to calculate the RVE problems.

In the initial intact state, responses of both mechanical and transport RVEs are linear. They can be therefore easily pre-computed resulting in a great computational cost reduction. If one is interested in macroscopic variables only, there is no need to reconstruct the fast field and pre-computed material matrix is sufficient. The linear pre-computed state is adaptively replaced by the full RVE non-linear problem with a help of Ottosen’s criterion [52] serving as an indicator of inelasticity. The decision process is implemented exactly as described in Ref. [57] for the mechanical homogenization, the transport RVE is replaced simultaneously.

The continuous macroscopic solution is approximated via the finite element method, development of the discretized weak form of Eqs. (30) is straightforward. Cosserat trilinear isoparametric brick elements extended by additional pressure degrees of freedom are used. The same trilinear shape functions are applied to approximate the element shape as well as the displacements, rotations and the pressure. The methodology for element implementation was adopted from Ref. [41]. Full Gauss integration using 8 integration points (hence 8 submodel RVE pairs for each element) is employed. Rezakhani and Cusatis [56] shows that the Cosserat components might be ignored with almost no price in accuracy, however such simplification is not implemented here.

7 Verification

The model is verified by four examples featuring concrete specimens: (i) Terzaghi’s consolidation, (ii) flow through a compressed cylinder, (iii) constrained tension of a sealed prism and (iv) hydraulic fracturing of a hollow cylinder. The examples specifically target different coupling terms in the macroscopic balance equations. All verification examples compare the *full* discrete model and the *homogenized* model. All four cases also share the same material mesostructure (described in the previous section) and constitutive model described in Appendix E, including the material parameters from Table 1.

The mesoscale discrete model exhibits intrinsic randomness due to random locations of aggregates. Even though the comparison should ideally be repeated several times for different realizations of concrete mesostructure, only single realization is used in all the examples. All the calculations are done on a single processor within a single thread. There is a huge potential to speed-up the *homogenized* model by distributing independent RVE problems over several processors. Such distributed solution is possible also for the *full* model by parallelizing solver of the system of linear equations, but efficiency is typically significantly lower.

7.1 Linear Terzaghi’s consolidation

The model is first verified by simulating Terzaghi’s consolidation. A prism of material of size $0.5 \times 0.1 \times 0.1$ m³ is initially under zero pressure and zeros strain. The x axis runs along its longest central axis, the domain begins at $x = 0$ m and ends at $x = 0.5$ m. The prism is sealed at all boundaries except the front end at $x = 0$ where pressure p^* is prescribed at time $t = 0$ and kept constant throughout the simulation. The mechanical boundary conditions prescribe zero rotations at all boundaries, zero x displacement at the rear end at $x = 0.5$ m and zero y and z displacements at all rectangular sides. Total traction t_x^* is prescribed at the front end at $x = 0$ and kept constant the whole simulation time. Biot coefficient $b = 0.5$ and reference pressure $p_0 = 0$ MPa; linear elastic material behavior is enforced.

Two cases are investigated. In the first case (denoted *loading by pressure*), the prescribed values read $p^* = 1$ MPa and $t_x^* = 0$ MPa. The pressure propagates along the x axis and transfers into mechanical forces through the Biot’s coupling leading to elongation of the prism. Prescribed values for the latter case (denoted *loading by traction*) read $p^* = 0$ MPa and $t_x^* = 1$ MPa. In this case the mechanical volumetric deformation induces a pressure increase that is released at the front end of the prism.

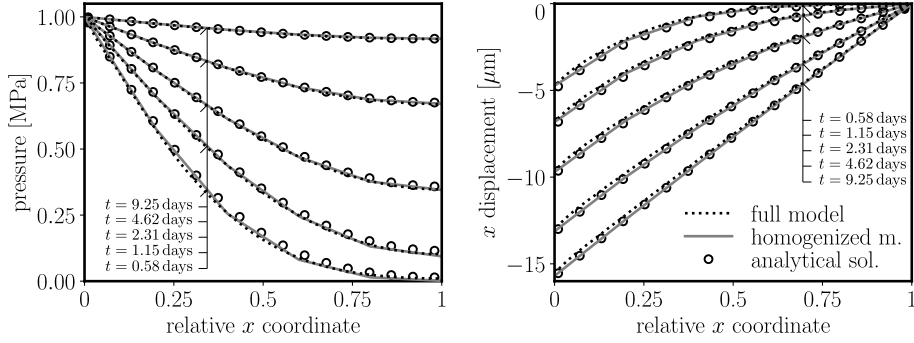


Figure 2: Terzaghi's consolidation, loading by fluid pressure: fluid pressure and x displacement profiles at various times of simulation as computed by the *homogenized* model (macroscopic component only) and the *full* model.

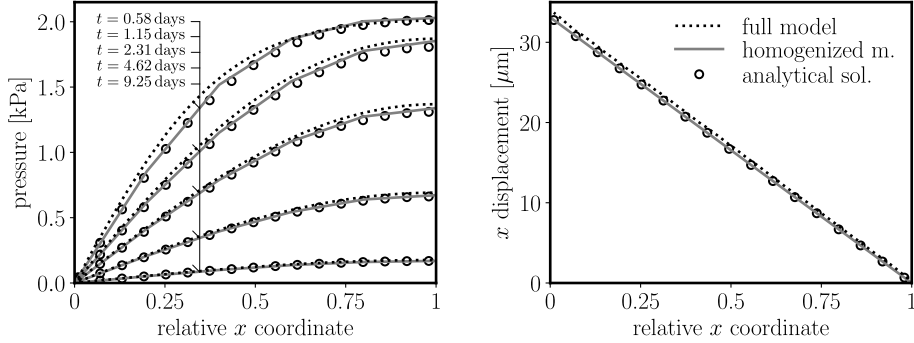


Figure 3: Terzaghi's consolidation, loading by traction: fluid pressure and x displacement profiles at various times of simulation as computed by the *homogenized* model (macroscopic component only) and the *full* model.

The problem is analyzed using the *full* discrete and *homogenized* continuous model. Five trilinear 8-node isoparametric finite elements of equal size along the x direction are used at macroscale. Comparison of both models in terms of pressure and x displacement profiles along the central x axis at different time instants is presented in Figs. 2 (loading by pressure) and 3 (loading by traction). Relatively small differences are attributed to (i) heterogeneity and (ii) boundary layer effect [26], or wall effect, that is present in the *full* model and modify the mechanical properties in the vicinity of the boundary.

The *full* model has approx 124,000 DoF and the computation took approximately 3 hours for pressure loading and 2.5 hours for traction loading case. On contrary, the *homogenized* model has only 40 DoF and calculation took approximately 1 s in both loading cases. The speed-up factor is about four orders of magnitude thanks to the enforced linearity of the RVE response, which can be pre-computed at the simulation initialization.

There exists an analytical solution to the problem [66, 23]. Pressure and displacement fields are provided by the functions listed in Appendix F. The analytical solution, added to Figs. 2 and 3, agrees well with the numerical model results.

7.2 Flow through compressed cylinder

The second verification example is steady state simulation of cylinder (depth 0.1 m, diameter 0.1 m) compressed in z direction assuming no friction taking place at the loading platens, i.e., the lateral expansion is completely unconstrained. Simultaneously, a pressure gradient is applied in z direction by prescribing pressure at the bottom face at $z = 0$ m being 1 MPa and at the top face at $z = 0.1$ m being 0 MPa. The normal flux component over the cylindrical shell is set to zero. The Biot coefficient is $b = 0$, hence the only coupling mechanism is the dependency of the permeability coefficient λ on normal crack opening.

The *homogenized* model consists of a single brick with 8 integration points. Depth of the brick is 0.1 m, upper and bottom faces are squares of size $0.05\sqrt{\pi} \times 0.05\sqrt{\pi}$ m² corresponding to the cylinder cross-sectional area. Each of the 8 RVE pairs is independent, initially pre-computed but later, after the Ottosen's criterion indicates it, represented by

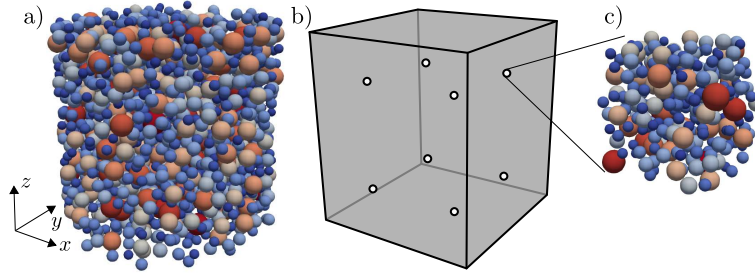


Figure 4: a) Cylindrical specimen, *full* model; b) single brick element, *homogenized* model; c) RVE attached to an integration point.

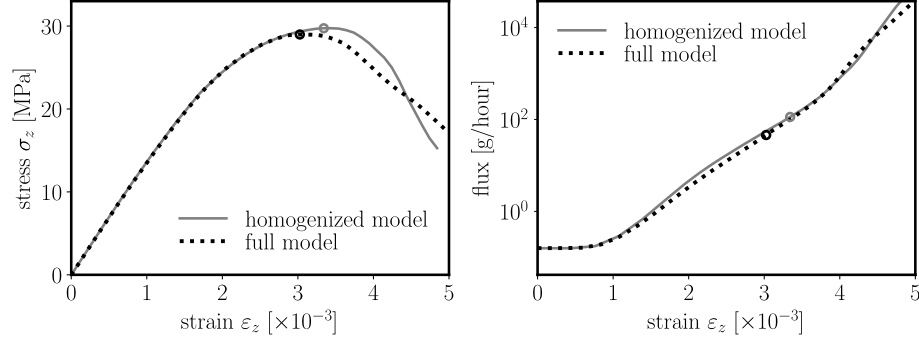


Figure 5: Loading traction and flux through cylindrical specimen obtained by the *full* and *homogenized* model. Circles label states at which the models reached the maximum loading force.

the full RVE problem. A sketch of the model is shown in Fig. 4. The macroscopic model consists of additional 8 free DoF. The *homogenized* model therefore has $8 \times (2,160 + 2,016) + 8 = 33,416$ DoF in total and runs in 25 min.

The *full* model has 32,500 DoF and runs in 68 min. Even though the number of DoF is similar, the speed-up factor is about 2.7. The improvement is caused by decoupling the systems into separate problems, hence speeding-up its solution.

Stresses and fluxes obtained by the *full* and *homogenized* model are similar, see Fig. 5. Since the constitutive model features strain softening, the mechanical problem suffers from strain localization. It is well known that the localization phenomenon cannot be homogenized as the scale separation does not hold [36]. Few research papers [16, 69] provide suggestions and remedies to capture strain localization properly in the homogenization scheme (see Sec. 1) but these are not used here. The reason why our verification study gives more or less satisfactory results even under strain localization is that the RVE volumes exactly correspond to the volumes of material represented by the associated integration points. Consequently, the strain localization occurs in the same material volumes in both models and should be therefore macroscopically equivalent. This shortcut was developed in Ref. [56] for the mechanical problem only, one can see that it is applicable also for the coupled problem. Unfortunately, the major benefit of homogenization, that the large material volume can be macroscopically represented by small RVE, is lost.

7.3 Constrained tension of a sealed prism

The third verification example is focused on coupling terms excluded in the previous two examples, specifically the effect of cracks on fluid stored in the transient simulation. The same prism as in the consolidation example 7.1 is used. To completely exclude complications with strain localization, the mechanical fields (displacement and rotations) are strongly constrained: three macroscopic degrees of freedom with meaning of macroscopic strains ε_x , ε_y and ε_z dictate displacement of all the particles while all the rotations are zero.

$$u_i = x_i \varepsilon_i \quad \theta_i = 0 \quad i \in \{x, y, z\} \quad (36)$$

The strain ε_x is prescribed, growing by rate $2 \times 10^{-8} \text{ s}^{-1}$, the other two strains are free. Stress σ_x is measured as conjugate variable to ε_x divided by the prism volume. The whole mechanical problem has only 2 degrees of freedom

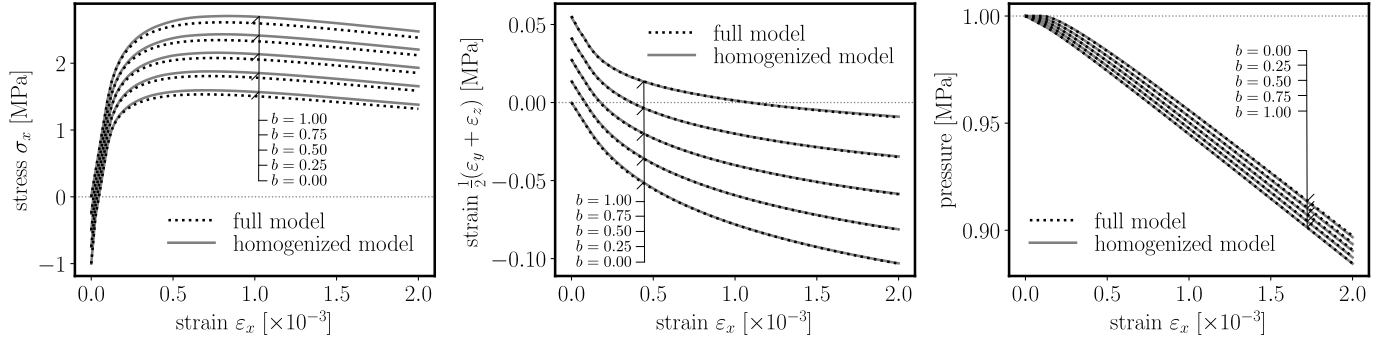


Figure 6: Evolution of stress σ_x , the average of lateral macroscopic strains and the average pressure in prism loaded by strain ε_x under Voigt's constraint.

(ε_y and ε_z) under such constraint. The transport problem is unconstrained and sealed, no flux is allowed between the prism domain and the surroundings. The initial pressure as well as the reference pressure p_0 are set to 1 MPa and the mechanical DoF ε_y and ε_z are initially set so that the model is in static equilibrium. Due to applied mechanical tension, the average pressure in the domain decreases and the prism shrinks in lateral direction. Simulations are performed with various values of the Biot coefficient b ranging from 0 to 1.

The Voigt's constraint described by Eq. (36) is applied also to the *homogenized* model at macroscale. The microscopic mechanical field must be zero everywhere, therefore all displacements and rotations at mechanical RVEs are zero (no free DoF is left). Note that the RVE cracks still develop due to the eigen-strains projected from the macroscale. Around 83,000 DoF are used for the transport part in the *full* model. 24 macroscopic pressure DoF are free in the *homogenized* model, summing with 40 transport RVEs of 2,160 DoF makes it $24 + 40 \times 2,160 = 86,424$ transport DoF in total. The average computation times for *full* or *homogenized* models are around 3 hours or 40 min, respectively. Speed-up factor 4.5 is again achieved by decoupling the system into individual RVE problems, even though the total number of DoF is comparable.

Figure 6 presents obtained axial macroscopic stress, lateral strain and the average pressure. There is an excellent agreement between the *full* and *homogenized* models, minor difference is seen in stress σ_x . This is again attributed to the wall effect present in the *full* model [26]. Note, that the lateral strains vary with Biot coefficient; apparent Poisson's ratio is strongly affected by the pressure of the fluid.

7.4 Hydraulic fracturing of hollow cylinder

The last example is meant as a simple application. The specimen is a hollow cylinder of depth 0.05 m, inner radius $r_i = 0.05$ m, outer radius $r_o = 0.3$ m. The cylinder central axis is align with axis z . Transport boundary conditions prescribe constant zero pressure at the outer cylinder shell, pressure linearly increasing in time $p_i = 200t$ at the inner surface and zero normal flux at the upper and bottom surfaces at $z = 0$ m and $z = 0.05$ m. Mechanical boundary conditions restrict z displacements at the upper and bottom surface and apply inward traction on the inner surface of a magnitude equal to the prescribed pressure.

The *full* model has approximately 323,000 DoF. The *homogenized* model was built in two versions. (i) The fine version is discretized into 15 elements equidistantly distributed in radial direction, 30 elements along the circumference and one element over the depth, resulting in 450 elements and 3600 RVEs. (ii) The coarse version has only 4 elements in radial direction and 10 element along circumference. In total, it has 40 element, 320 RVEs and approx. $320 \times (2,160 + 2,016) \approx 1.3$ mil. DoF, assuming all the RVEs are switched from pre-computed to inelastic states.

Let us first verify that the model provides the correct steady state elastic solution. Figure 7 shows relative pressure and displacement profiles along the radial direction, r is a distance from the central axis of the cylinder. Both fine and coarse *homogenized* models are used, their results are obtain in almost no time (about 5 s and 3 s, respectively) because RVE responses can be pre-computed. The *full* model computation takes about 13 min, speed up factor is 2–3 orders of magnitude. Results of the coarse model suffer from poor macroscopic approximation, but even these seems relatively close to the *full* model data.

The analytical solution to the elastic problem is derived in Ref. [37], see Appendix G. It is shown in Fig. 7 along with the numerical results. The agreement is good for all considered Biot coefficient values.

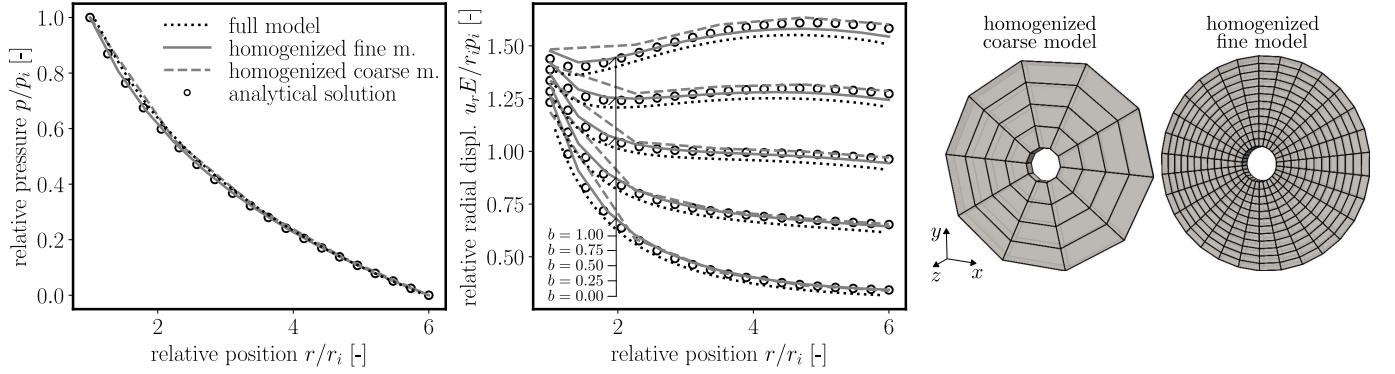


Figure 7: Pressure and radial displacement profiles from the elastic simulations of the pressurized hollow cylinder. The analytical solution is taken from Ref. [37]. Meshes used for the *homogenized* coarse and fine models are sketched on the right-hand side.

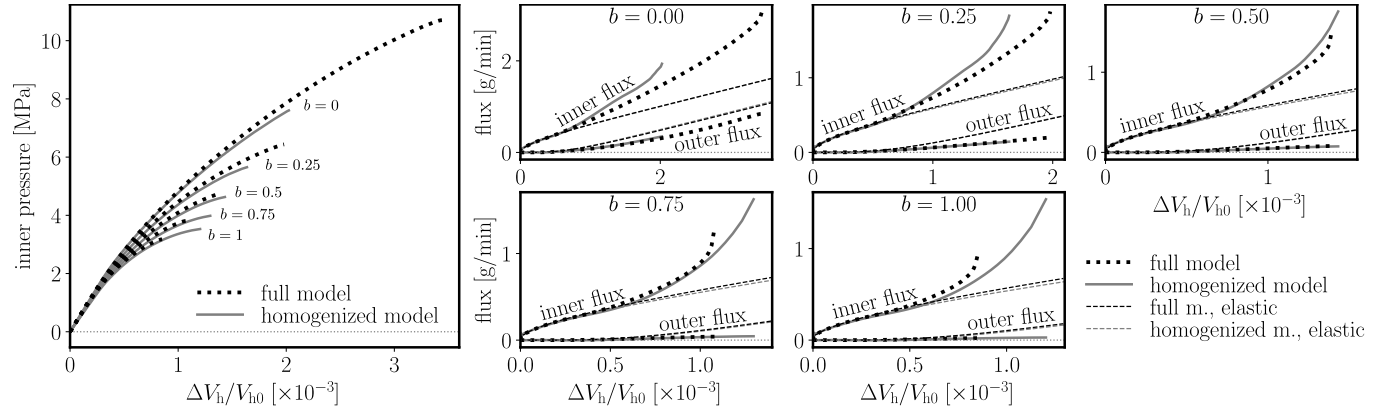


Figure 8: Pressure in the hole and inner and outer fluxes obtained during simulation of hydraulic fracturing. The horizontal axis shows relative volumetric change of the central hole of initial volume V_{h0} , ΔV_h denotes absolute volume change.

The inelastic transient behavior is simulated next. Initial and reference pressures are set to zero. Simulation is controlled by increase of the inner pressure, p_i ; therefore it eventually reaches the critical maximum pressure at which macroscopic cracks develop across the whole cylinder and solver fails due to loss of convergence. Another complication arises in *homogenized* models because the macroscopic crack may develop in any direction. Standard periodic boundary conditions cannot handle such situation [64] and advanced approach is needed [17]. Instead, the RVEs are rotated in this study so they are all aligned with the radial direction under which the crack is expected. Such a remedy is acceptable for this particular example but cannot be used for a general case where the crack direction is unknown.

Change of the volume of the central hole, ΔV_h , inner flux and outer flux are recorder during the simulation. The results are shown in Fig. 8. A reasonable correspondence in terms of pressures/tractions and fluxes is obtained. The larger differences occurring in the later stages of the simulations are attributed to the developed strain localization. The RVE volumes of the *homogenized* model are actually much larger than the macroscopic material volumes associated with integration points. Unfortunately, the localized cracks significantly affect the solution and cause deviations of the homogenized model results from the reference *full* solution. Note that Fig. 8 shows also fluxes obtained from elastic simulations to visualize the effect of cracking on the flux as a difference between elastic and inelastic solutions.

Figure 9 shows cracks developed in the *full* and *homogenized* models. One can see localized macrocracks developed in the *full* model. The internal structure of the *full* model (positions of particles) is constant, that is why the macrocracks tend to appear at the same locations, presumably at some locally weaker region. On the contrary, the *homogenized* model possesses an ideal symmetry and strain localization at the macroscale occurs in a random direction due to the numerical truncation. No strain localization has been achieved for *homogenized* models with Biot's

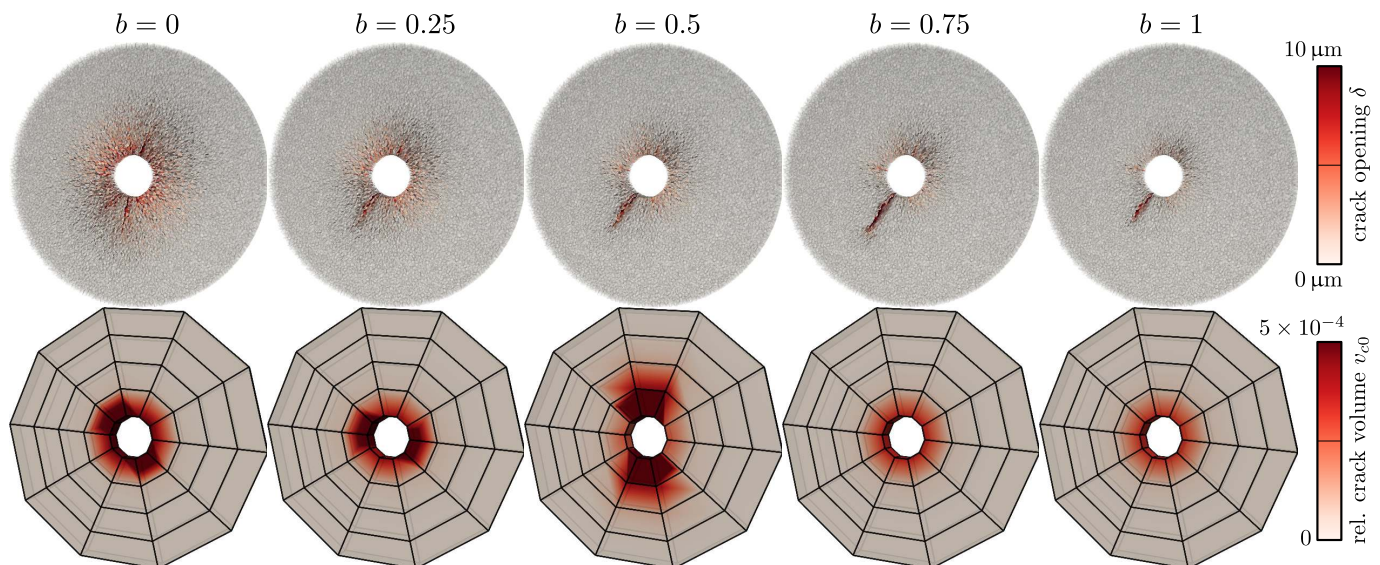


Figure 9: Cracks developed in the *full* and *homogenized* models at the last valid step of the simulation.

coefficients 0.75 and 1, the symmetry was maintained until the last simulation step. The symmetry can be effectively impaired by either generating several different RVE mesostructures or randomly changing material parameters of otherwise identical RVEs.

Interestingly enough, the cracking character changes with Biot coefficient. There is more diffused microcracking appearing at the critical pressure around the central hole for low Biot coefficients. This is due to different pressure magnitude sustained by models with different Biot coefficient. If one studies the cracking at the same pressure level, the situation is actually the opposite: the larger Biot coefficients give more diffused cracking because the fluid pressure reduces both radial and circumferential compressive stresses in the solid. Since it further helps to open the cracks, the critical pressure for larger Biot coefficients is substantially lower.

The *full* model simulations took 2970 min, 2290 min, 1220 min, 980 min and 730 min for Biot coefficients 0, 0.25, 0.5, 0.75 and 1, respectively. Only the coarse *homogenized* model was employed in the inelastic analyses reaching computational times 330 min, 250 min, 150 min, 132 min and 120 min and speed-up factors about 9, 9.2, 8.1, 7.4 and 6.1, respectively. This is surprising considering that the *homogenized* model has about 4 times more DoF when all RVEs leave the pre-computed state. The high speed-up factors are achieved by decoupling the system of equations into independent subsystems and also by keeping many RVEs in their pre-computed state for most of the simulation time.

8 Conclusions

Asymptotic expansion homogenization of discrete mesoscale models for coupled mechanics and mass transport in a fully saturated heterogeneous medium is developed. Coupling is provided by Biot's theory and an effect of cracks on material permeability coefficient. Based on the results obtained in this study the following conclusions can be drawn.

- The macroscale problem arising from the homogenization is described by the standard transient transport and Cosserat continuous differential equations enriched by coupling terms. The macroscopic problem can be solved with a help of the finite element method by transforming it into the weak form. The constitutive equation routines are replaced by subscale RVE problems. The homogenized macroscopic material exhibits naturally anisotropy due to cracking at the microscale, both for the mass transport and mechanical behavior.
- The microscale problems are discrete and steady state; the mechanical RVE is independent on the transport RVE while the transport RVE requires information about crack openings from the mechanical RVE. Therefore, they can be solved sequentially.
- Microscale periodic RVE problems are loaded by projection of macroscopic strain and pressure gradient tensors

into eigen-strains and eigen-pressure gradients of the discrete elements. The homogenization procedure derives expressions for macroscopic stress, couple stress and flux as a summation of certain quantities from the discrete elements. These summation formulas correspond to the known expressions used for discrete systems in the literature.

- Homogenization techniques derived earlier for pure momentum balance [56] or pure mass transport [29] emerge from the homogenized coupled system when the coupling terms are removed.
- Simplifications are possible for a special type of tessellation where normal and contact vectors are parallel, e.g., for Voronoi or power/Laguerre tessellations. Several terms at macro and microscale disappear or become simpler.
- The homogenization technique is applied to a discrete mesoscale model of concrete. Several examples specifically targeting different terms of the coupling structure are provided demonstrating correspondence between the *full* and *homogenized* model responses. An additional verification is supplied by comparing the result to the analytical solution, if available. The last example verifying the homogenized equations features hydraulic fracturing of a hollow cylinder.
- Speed-up factors of several orders of magnitude can be obtained for elastic problems for which the RVE responses can be pre-computed. Significant time savings can also be achieved for inelastic simulations. All the comparisons were computed as single thread processes. It is expected that further improvement would be gained, should they run distributed on several computational cores in parallel because the RVE problems from different integration points can be solved independently.
- The major unsolved problem is strain localization because it violates the fundamental homogenization assumptions and the RVE ceases to exist. The microscale problem becomes size dependent. Recent developments showing remedies to overcome this issue are discussed but not implemented in this study. This issue remains open for further investigation.

A Expansion of pressure gradient, strain and curvature

The following equations provide individual terms of expansions of the pressure gradient g , strain ε and curvature χ of the discrete model used in Eq. (17).

$$g^{(-2)} = \frac{1}{\bar{h}} [p^{-1Q} - p^{-1P}] \quad (37a)$$

$$g^{(-1)} = \frac{1}{\bar{h}} \left[p^{0Q} + \frac{\partial p^{-1Q}}{\partial X_i} y_i^{PQ} - p^{0P} \right] \quad (37b)$$

$$g^{(0)} = \frac{1}{\bar{h}} \left[p^{1Q} + \frac{\partial p^{0Q}}{\partial X_i} y_i^{PQ} + \frac{1}{2} \frac{\partial^2 p^{-1Q}}{\partial X_i X_j} y_i^{PQ} y_j^{PQ} - p^{1P} \right] \quad (37c)$$

$$g^{(1)} = \frac{1}{\bar{h}} \left[\frac{\partial p^{1Q}}{\partial X_i} y_i^{PQ} + \frac{1}{2} \frac{\partial^2 p^{0Q}}{\partial X_i X_j} y_i^{PQ} y_j^{PQ} + \frac{1}{6} \frac{\partial^3 p^{-1Q}}{\partial X_i X_j X_k} y_i^{PQ} y_j^{PQ} y_k^{PQ} \right] \quad (37d)$$

$$\varepsilon_\alpha^{(-1)} = \frac{e_i^\alpha}{\bar{l}} [u_i^{0J} - u_i^{0I} + \varepsilon_{ijk} \omega_j^{-1J} \tilde{c}_k^J - \varepsilon_{ijk} \omega_j^{-1I} \tilde{c}_k^I] \quad (37e)$$

$$\varepsilon_\alpha^{(0)} = \frac{e_i^\alpha}{\bar{l}} \left[u_i^{1J} - u_i^{1I} + \frac{\partial u_i^{0J}}{\partial X_j} y_j^{IJ} + \varepsilon_{ijk} \left(\omega_j^{0J} + \varphi_j^{0J} + \frac{\partial \omega_j^{-1J}}{\partial X_m} y_m^{IJ} \right) \tilde{c}_k^J - \varepsilon_{ijk} \left(\omega_j^{0I} + \varphi_j^{0I} \right) \tilde{c}_k^I \right] \quad (37f)$$

$$\varepsilon_\alpha^{(1)} = \frac{e_i^\alpha}{\bar{l}} \left[\frac{\partial u_i^{1J}}{\partial X_j} y_j^{IJ} + \frac{1}{2} \frac{\partial^2 u_i^{0J}}{\partial X_j X_k} y_j^{IJ} y_k^{IJ} + \varepsilon_{ijk} \left(\varphi_j^{1J} + \frac{\partial (\omega_j^{0J} + \varphi_j^{0J})}{\partial X_m} y_m^{IJ} + \frac{1}{2} \frac{\partial^2 \omega_j^{-1J}}{\partial X_m X_n} y_m^{IJ} y_n^{IJ} \right) \tilde{c}_k^J - \varepsilon_{ijk} \varphi_j^{1I} \tilde{c}_k^I \right] \quad (37g)$$

$$\chi_\alpha^{(-2)} = \frac{e_i^\alpha}{\bar{l}} [\omega_i^{-1J} - \omega_i^{-1I}] \quad (37h)$$

$$\chi_\alpha^{(-1)} = \frac{e_i^\alpha}{\bar{l}} \left[\omega_i^{0J} + \varphi_i^{0J} + \frac{\partial \omega_i^{-1J}}{\partial X_j} y_j^{IJ} - \omega_i^{0I} - \varphi_i^{0I} \right] \quad (37i)$$

$$\chi_\alpha^{(0)} = \frac{e_i^\alpha}{\bar{l}} \left[\varphi_i^{1J} + \frac{\partial (\omega_i^{0J} + \varphi_i^{0J})}{\partial X_j} y_j^{IJ} + \frac{1}{2} \frac{\partial^2 \omega_i^{-1J}}{\partial X_j X_k} y_j^{IJ} y_k^{IJ} - \varphi_i^{1I} \right] \quad (37j)$$

The terms with higher η power are omitted as they are negligibly small.

B Taylor series of flux, traction, couple traction and moment of traction

The second nonzero components of stress-like variables are derived via Taylor series. The flux (or more precisely the permeability coefficient λ) is expanded around points $p = p_\lambda^{(0)}$, $\delta = \eta \delta_\lambda^{(1)}$, traction \mathbf{t} and moment of traction \mathbf{w} around points $\varepsilon = \varepsilon^{(0)}$, $p = p_a^{(0)}$ and couple traction \mathbf{m} around point $\chi = \eta^{-1} \chi^{(-1)}$, respectively.

$$\eta j^{(1)} \approx -\eta p_\lambda^{(1)} g^{(0)} \frac{\partial \lambda(p, \delta)}{\partial p} \Big|_{\substack{p=p_\lambda^{(0)} \\ \delta=\eta \delta_\lambda^{(1)}}} - \eta^2 \delta_\lambda^{(2)} g^{(0)} \frac{\partial \lambda(p, \delta)}{\partial \delta} \Big|_{\substack{p=p_\lambda^{(0)} \\ \delta=\eta \delta_\lambda^{(1)}}} - \lambda(p_\lambda^{(0)}, \eta \delta_\lambda^{(1)}) \eta g^{(1)} \quad (38a)$$

$$= \eta \frac{\partial j^{(0)}}{\partial p_\lambda^{(0)}} p_\lambda^{(1)} + \eta \frac{\partial j^{(0)}}{\partial \delta_\lambda^{(1)}} \delta_\lambda^{(2)} + \eta \frac{\partial j^{(0)}}{\partial g^{(0)}} g^{(1)}$$

$$\eta t_\alpha^{(1)} \approx \eta \varepsilon_\beta^{(1)} \frac{\partial t_\alpha(\varepsilon, p)}{\partial \varepsilon_\beta} \Big|_{\substack{\varepsilon=\varepsilon^{(0)} \\ p=p_a^{(0)}}} + \eta p^{(1)} \frac{\partial t_\alpha(\varepsilon, p)}{\partial p} \Big|_{\substack{\varepsilon=\varepsilon^{(0)} \\ p=p_a^{(0)}}} = \eta \frac{\partial t_\alpha^{(0)}}{\partial \varepsilon_\beta^{(0)}} \varepsilon_\beta^{(1)} + \eta \frac{\partial t_\alpha^{(0)}}{\partial p_a^{(0)}} p_a^{(1)} \quad (38b)$$

$$\eta^2 m_\alpha^{(2)} \approx \chi_\beta^{(0)} \frac{\partial m_\alpha(\chi)}{\partial \chi_\beta} \Big|_{\chi=\eta^{-1} \chi^{(-1)}} = \eta^2 \frac{\partial m_\alpha^{(1)}}{\partial \chi_\beta^{(-1)}} \chi_\beta^{(0)} \quad (38c)$$

$$\eta^2 w_i^{(2)} \approx \eta \varepsilon_\beta^{(1)} \frac{\partial w_i(\varepsilon, p)}{\partial \varepsilon_\beta} \Big|_{\substack{\varepsilon=\varepsilon^{(0)} \\ p=p_a^{(0)}}} + \eta p^{(1)} \frac{\partial w_i(\varepsilon, p)}{\partial p} \Big|_{\substack{\varepsilon=\varepsilon^{(0)} \\ p=p_a^{(0)}}} = \eta^2 \frac{\partial w_i^{(1)}}{\partial \varepsilon_\beta^{(0)}} \varepsilon_\beta^{(1)} + \eta^2 \frac{\partial w_i^{(1)}}{\partial p_a^{(0)}} p_a^{(1)} \quad (38d)$$

C Macroscale: from discrete to continuous representation

Balance equations (29) are summed over the whole RVE. The summations are straightforward in the case of fluxes (Eq. 29a) and linear momentum (Eq. 29b). In the case of angular momentum (Eq. 29c), one must select some reference point in the global reference system \mathbf{X} and sum all the moment contributions with respect to that particular point. It is convenient to choose the origin of reference system \mathbf{X} , therefore the distances to this reference point from an arbitrary point \mathbf{x}_r inside RVE will always have two components: $\mathbf{X}_r = \mathbf{X}_{\text{RVE}} + \mathbf{x}_r$, the first component being the location of the RVE centroid in the global reference system, the latter is the position within the RVE. The moment due to inertia must be updated since the reference point is now changed to the origin of the \mathbf{X} reference system. An analogy to Eq. (5) with a different reference point is used, $\mathbf{u}^{(0)}$ is constant and $\sum_{I \in V_0} \rho V (\mathbf{X}_{\text{RVE}} + \mathbf{x}_I + \mathbf{r}_0) = \langle \rho \rangle V_0 \mathbf{X}_{\text{RVE}}$ because \mathbf{X}_{RVE} is the RVE centroid

$$\sum_{I \in V_0} \mathbf{M}_{ub}^T \cdot \ddot{\mathbf{u}}^{(0)} = \left[\sum_{I \in V_0} \rho V \mathcal{E} \cdot (\mathbf{X}_{\text{RVE}} + \mathbf{x}_I + \mathbf{r}_0) \right] \cdot \ddot{\mathbf{u}}^{(0)} = \langle \rho \rangle V_0 \mathcal{E} : (\mathbf{X}_{\text{RVE}} \otimes \ddot{\mathbf{u}}^{(0)}) \quad (39)$$

Also the moment due to external load \mathbf{b} acting in the RVE centroid is added. The three balance equations (29) are transformed into

$$\frac{\eta}{V_0} \sum_{P \in V_0} \sum_{Q \in W} S^* j^{(1)} = \rho_{w0} \left[\dot{v}_{c0} \left(1 - b + \frac{p^{(0)} - p_0}{K_w} \right) + v_{c0} \frac{\dot{p}^{(0)}}{K_w} + 3b \dot{\varepsilon}_V^{(0)} + \frac{\dot{p}^{(0)}}{M_b} \right] + q \quad (40a)$$

$$\frac{\eta}{V_0} \sum_{I \in V_0} \sum_{J \in V} A^* t_\alpha^{(1)} \mathbf{e}_\alpha = \langle \rho \rangle \ddot{\mathbf{u}}^{(0)} - \mathbf{b} \quad (40b)$$

$$\frac{\eta^2}{V_0} \sum_{I \in V_0} \sum_{J \in V} A^* \left(\mathbf{w}^{(2)} + m_\alpha^{(2)} \mathbf{e}_\alpha \right) = \langle \rho \rangle \mathcal{E} : (\mathbf{X}_{\text{RVE}} \otimes \ddot{\mathbf{u}}^{(0)}) - \mathcal{E} : (\mathbf{X}_{\text{RVE}} \otimes \mathbf{b}) \quad (40c)$$

New variable v_{c0} denoting the crack volume density in the whole RVE is introduced into the first equation (40a) for sake of simplicity

$$v_{c0} = \frac{1}{V_0} \sum_{P \in V_0} \sum_{Q \in W} v_c^{(0)} W = \langle v_c^{(0)} \rangle \quad (41)$$

Equations (38) are now substituted into the balance equations (40)

$$\frac{\eta}{V_0} \sum_{P \in V_0} \sum_{Q \in W} S^* \left(\frac{\partial j^{(0)}}{\partial p^{(0)}} p_\lambda^{(1)} + \frac{\partial j^{(0)}}{\partial \delta^{(0)}} \delta_\lambda^{(1)} + \frac{\partial j^{(0)}}{\partial g^{(0)}} g^{(1)} \right) = \rho_{w0} \left[\dot{v}_{c0} \left(1 + b + \frac{p^{(0)} - p_0}{K_w} \right) \right. \quad (42a)$$

$$\left. + v_{c0} \frac{\dot{p}^{(0)}}{K_w} + 3b \dot{\varepsilon}_V^{(0)} + \frac{\dot{p}^{(0)}}{M_b} \right] + q \quad (42b)$$

$$\frac{\eta}{V_0} \sum_{I \in V_0} \sum_{J \in V} A^* \left(\frac{\partial t_\alpha^{(0)}}{\partial \varepsilon_\beta^{(0)}} \varepsilon_\beta^{(1)} + \frac{\partial t_\alpha^{(0)}}{\partial p^{(0)}} p_a^{(1)} \right) \mathbf{e}_\alpha = \langle \rho \rangle \ddot{\mathbf{u}}^{(0)} - \mathbf{b} \quad (42c)$$

$$\frac{\eta^2}{V_0} \sum_{I \in V_0} \sum_{J \in V} A^* \left(\frac{\partial \mathbf{w}^{(1)}}{\partial \varepsilon_\beta^{(0)}} \varepsilon_\beta^{(1)} - \frac{\partial \mathbf{w}^{(1)}}{\partial p^{(0)}} p_a^{(1)} + \frac{\partial m_\alpha^{(1)}}{\partial \chi_\beta^{(-1)}} \chi_\beta^{(0)} \right) \mathbf{e}_\alpha = \mathcal{E} : \left[\mathbf{X}_{\text{RVE}} \otimes \left(\langle \rho \rangle \ddot{\mathbf{u}}^{(0)} - \mathbf{b} \right) \right] \quad (42d)$$

Each element on the left-hand side appears in the summation twice, once connecting node I with node J and once connecting J with I (or P with Q , respectively). The contact vectors of these two identical element have opposite directions ($\mathbf{x}_{IJ} = -\mathbf{x}_{JI}$, $\mathbf{x}_{PQ} = -\mathbf{x}_{QP}$). Also their directional vectors have opposite sign (${}^I \mathbf{e}_\alpha = -{}^J \mathbf{e}_\alpha$). The tractions $t_\alpha^{(0)}$, strains $\varepsilon_\alpha^{(0)}$, pressures $p^{(-1)}$, average pressures $p_a^{(1)}$ and $p_\lambda^{(1)}$, normal crack openings $\delta_\lambda^{(0)}$ and $\delta_\lambda^{(1)}$, couple tractions $m_\alpha^{(1)}$ and curvatures $\chi_\beta^{(-1)}$ are identical, moments of traction $w^{(1)}$ as well as fluxes $j^{(-1)}$ and pressure gradients $g^{(-1)}$ have the same magnitude but opposite direction.

Three terms with $p^{(1)}$ and one with $\delta_\lambda^{(1)}$ disappear from Eqs. (42) as the same expressions are subtracted. The remaining terms lead to summation of two pressure gradients and subtraction of strains and curvatures of those two

identical elements, which according to Eqs. (37d), (37g) and (37j) read (using $\boldsymbol{\omega}^{(-1)} = \mathbf{0}$; $p^{(0)}$, $\mathbf{u}^{(0)}$ and $\boldsymbol{\varphi}^{(0)}$ are constants)

$${}^{PQ}g^{(1)} + {}^{QP}g^{(1)} = \frac{1}{\bar{h}} \left[\frac{\partial (p^{1Q} - p^{1P})}{\partial X_i} y_i^{PQ} + \frac{\partial^2 p^{(0)}}{\partial X_i \partial X_j} y_i^{PQ} y_j^{PQ} \right] = \frac{\partial g^{(0)}}{\partial X_i} y_i^{PQ} \quad (43a)$$

$$\begin{aligned} {}^{IJ}\varepsilon_\beta^{(1)} - {}^{JI}\varepsilon_\beta^{(1)} &= \frac{e_i^\beta}{\bar{l}} \left[\frac{\partial (u_i^{1J} - u_i^{1I})}{\partial X_j} y_j^{IJ} + \varepsilon_{ijk} \left(\frac{\partial (\omega_j^{0J} + \varphi_j^{(0)})}{\partial X_m} \tilde{c}_k^J - \frac{\partial (\omega_j^{0I} + \varphi_j^{(0)})}{\partial X_m} \tilde{c}_k^I \right) y_m^{IJ} \right. \\ &\quad \left. + \frac{\partial^2 u_i^{(0)}}{\partial X_j \partial X_k} y_j^{IJ} y_k^{IJ} \right] = \frac{\partial \varepsilon_\beta^{(0)}}{\partial X_i} y_i^{IJ} \end{aligned} \quad (43b)$$

$${}^{IJ}\chi_\beta^{(0)} - {}^{JI}\chi_\beta^{(0)} = \frac{e_i^\beta}{\bar{l}} \left[\frac{\partial (\omega_i^{0J} + \varphi_i^{(0)} - \omega_i^{0I} - \varphi_i^{(0)})}{\partial X_j} y_j^{IJ} \right] = \frac{\partial \chi_\beta^{(-1)}}{\partial X_i} y_i^{IJ} \quad (43c)$$

Equations (43) are substituted back to the Eqs. (42) along with application of the chain rule, replacement of the double summation to single summation over all the elements and change from \mathbf{y}_{IJ} to \mathbf{x}_{IJ}/η to obtain

$$\frac{1}{V_0} \sum_{d \in V_0} S^* \frac{\partial j^{(0)}}{\partial X_i} x_i^{PQ} = \rho_{w0} \left[\dot{v}_{c0} \left(1 - b + \frac{p^{(0)} - p_0}{K_w} \right) + v_{c0} \frac{\dot{p}^{(0)}}{K_w} + 3b\dot{\varepsilon}_V^{(0)} + \frac{\dot{p}^{(0)}}{M_b} \right] + q \quad (44a)$$

$$\frac{1}{V_0} \sum_{e \in V_0} A^* \frac{\partial t_\alpha^{(0)}}{\partial X_i} x_i^{IJ} \mathbf{e}_\alpha = \langle \rho \rangle \ddot{\mathbf{u}}^{0I} - \mathbf{b} \quad (44b)$$

$$\frac{\eta}{V_0} \sum_{e \in V_0} A^* \left(\frac{\partial \mathbf{w}^{(1)}}{\partial X_i} x_i^{IJ} + \frac{\partial m_\alpha^{(1)}}{\partial X_i} x_i^{IJ} \mathbf{e}_\alpha \right) = \boldsymbol{\varepsilon} : \left(\mathbf{X}_{\text{RVE}} \otimes \left(\langle \rho \rangle \ddot{\mathbf{u}}^{(0)} - \mathbf{b} \right) \right) \quad (44c)$$

The expression for derivative of the moment of traction $\eta \mathbf{w}^{(1)} = t_\alpha^{(0)} \boldsymbol{\varepsilon} : (\mathbf{X}_c \otimes \mathbf{e}_\alpha)$ is modified by substituting the position of the integration point $\mathbf{X}_c = \mathbf{X}_{\text{RVE}} + \mathbf{x}_c$

$$\eta \frac{\partial \mathbf{w}^{(1)}}{\partial X_n} = \varepsilon_{ijk} \frac{\partial (t_\alpha^{(0)} (X_j^{\text{RVE}} + x_j^c) e_k^\alpha)}{\partial X_n} = \varepsilon_{ijk} \frac{\partial (t_\alpha^{(0)} x_j^c e_k^\alpha)}{\partial X_n} + \varepsilon_{ijk} \frac{\partial t_\alpha^{(0)}}{\partial X_n} X_j^{\text{RVE}} e_k^\alpha + \varepsilon_{ink} t_\alpha^{(0)} e_k^\alpha \quad (45)$$

Thanks to periodicity of the RVE geometry providing $\partial x_i^{IJ}/\partial X_j = \partial e_i^\alpha/\partial X_j = \partial A^*/\partial X_j = 0$, variables x_{IJ} , \mathbf{e}_α and A^* can be moved inside or outside the differentiation with respect to \mathbf{X} . It allows one to define the following quantities called total macroscopic stress and total couple stress tensors

$$\boldsymbol{\sigma}_t = \frac{1}{V_0} \sum_{e \in V_0} l A^* t_\alpha^{(0)} \mathbf{e}_N \otimes \mathbf{e}_\alpha \quad (46a)$$

$$\boldsymbol{\mu}_t = \frac{1}{V_0} \sum_{e \in V_0} l A^* \mathbf{e}_N \otimes \left(\eta m_\alpha^{(1)} \mathbf{e}_\alpha + t_\alpha^{(0)} \boldsymbol{\varepsilon} : (\mathbf{x}_c \otimes \mathbf{e}_\alpha) \right) \quad (46b)$$

and rewrite the mechanical balance equations (44b) and (44c) accordingly

$$\nabla_X \cdot \boldsymbol{\sigma}_t = \langle \rho \rangle \ddot{\mathbf{u}}^{(0)} - \mathbf{b} \quad (47a)$$

$$\nabla_X \cdot \boldsymbol{\mu}_t + \boldsymbol{\varepsilon} : \boldsymbol{\sigma}_t = \boldsymbol{\varepsilon} : \left[\mathbf{X}_{\text{RVE}} \otimes \left(\langle \rho \rangle \ddot{\mathbf{u}}^{(0)} - \mathbf{b} - \nabla_X \cdot \boldsymbol{\sigma}_t \right) \right] \quad (47b)$$

The last term of the second equation is zero because its inner part exactly correspond to the first equation. Equations (44a), (46) and (47) can now be easily rewritten to Eqs. (30) and (31).

D Volumetric strain expansion

Equation (29a) features term $\varepsilon_V^{(0)}$. Volumetric strain is defined in Sec. (2) as one third of relative change of the tetrahedron volume. Let us denote four vertices of tetrahedron as a - d , areas and outward normals of faces opposite

to these vertices as A_a - A_d and \mathbf{n}_a - \mathbf{n}_d , respectively. The volumetric strain can be calculated as

$$\varepsilon_V = -\frac{1}{9\tilde{V}} \sum_{I=a\dots d} A_I \mathbf{u}_I \cdot \mathbf{n}_I \quad (48)$$

The negative sign is included since the normals are in the outward direction. Re-introducing the expansions from Eqs. (14b), (15b) and (18a), one arrives at

$$\varepsilon_V^{(0)} = -\frac{1}{9\tilde{V}} \sum_{I=a\dots d} \tilde{A}_I u_i^I n_i^I - \hat{\varepsilon}_V^{(0)} \quad \text{with} \quad \hat{\varepsilon}_V^{(0)} = \frac{1}{9\tilde{V}} \sum_{I=a\dots d} \tilde{A}_I \frac{\partial u_i^{(0)}}{\partial X_j} y_j^{dI} n_i^I \quad (49)$$

where we randomly chose one of the vertices as the primary one (d) and use it in the Taylor series to estimate displacements in other vertices.

Let us now further focus on the eigen part coming from the macroscopic displacement gradient. Since the gradient of displacements is constant over the RVE, it can be moved in front of the summation. The normal \mathbf{n}_a can be computed as the normalized cross product of vectors pointing from d to b and c : $n_i^a = \mathcal{E}_{ilm} y_l^{db} y_m^{dc} / 2\tilde{A}_a$. One therefore reads

$$\hat{\varepsilon}_V^{(0)} = \frac{1}{9\tilde{V}} \frac{\partial u_i^{(0)}}{\partial X_j} \sum_{I \in \{a,b,c\}} y_j^{dI} n_i^I A_I = \frac{1}{18\tilde{V}} \frac{\partial u_i^{(0)}}{\partial X_j} \delta_{ij} \mathcal{E}_{klm} y_k^{da} y_l^{db} y_m^{dc} = -\frac{1}{3} \frac{\partial \mathbf{u}^{(0)}}{\partial \mathbf{X}} : \mathbf{1} = \frac{1}{3} \text{tr} \left(\nabla \mathbf{u}^{(0)} \right) \quad (50)$$

The second equality substitutes the normal \mathbf{n}_I and re-arranges the multiplications and the third equality uses well known formula for the tetrahedron volume based on the determinant $\mathcal{E}_{klm} y_k^{da} y_l^{db} y_m^{dc} = -6\tilde{V}$. The eigen part of volumetric strain becomes one third of the macroscopic displacement gradient trace, i.e., the volumetric part of the macroscopic strain.

E Constitutive relations

The mechanical constitutive model relates mechanical strain vector $\boldsymbol{\varepsilon}$ to traction in the solid, $\mathbf{s} = f_s(\boldsymbol{\varepsilon})$. It is formulated in local coordinate system distinguishing normal (N) and two tangential (M and L) directions. The formulation is adopted from Ref. [20] and simplified by omitting the confinement effect, assuming non-decreasing damage also in compression and reducing number of material parameters to 4: normal elastic constant E_0 , tangential/normal stiffness ratio α , tensile strength f_t and tensile fracture energy G_t .

Normal and tangential tractions read

$$s_N = (1-d)E_0\varepsilon_N \quad s_M = (1-d)E_0\alpha\varepsilon_M \quad s_L = (1-d)E_0\varepsilon_L \quad (51)$$

d is non-decreasing damage parameter ranging from 0 (healthy material) to 1 (completely damaged material). If increasing, it is updated via equivalent boundary traction, s_{eq} , and equivalent strain, ε_{eq} , as $d = 1 - \frac{s_{\text{eq}}}{E_0\varepsilon_{\text{eq}}}$. Equivalent strain is defined as $\varepsilon_{\text{eq}} = \sqrt{\varepsilon_N^2 + \alpha\varepsilon_T^2}$, $\varepsilon_T = \sqrt{\varepsilon_M^2 + \varepsilon_L^2}$. Let us also define direction of straining ω evaluated from $\tan \omega = \varepsilon_N / \sqrt{\alpha}\varepsilon_T$. The equivalent boundary traction reads

$$s_{\text{eq}} = f_{\text{eq}} \exp \left(\frac{K}{f_{\text{eq}}} \left\langle \chi - \frac{f_{\text{eq}}}{E_0} \right\rangle \right) \quad (52)$$

The angled brackets return the positive part, f_{eq} denotes equivalent strength, K is the initial slope in the nonlinear regime and χ represents the loading history

$$f_{\text{eq}} = \begin{cases} \frac{16f_t}{\sqrt{\sin^2 \omega + \alpha \cos^2 \omega}} & \omega < \omega_0 \\ f_t \frac{4.52 \sin \omega - \sqrt{20.0704 \sin^2 \omega + 9\alpha \cos^2 \omega}}{0.04 \sin^2 \omega - \alpha \cos^2 \omega} & \omega \geq \omega_0 \end{cases} \quad (53)$$

$$K = \begin{cases} 0.26E_0 \left[1 - \left(\frac{\omega + \pi/2}{\omega_0 + \pi/2} \right)^2 \right] & \omega < \omega_0 \\ -K_t \left[1 - \left(\frac{\omega - \pi/2}{\omega_0 - \pi/2} \right)^{n_t} \right] & \omega \geq \omega_0 \end{cases} \quad (54)$$

$$\chi = \begin{cases} \varepsilon_{\text{eq}} & \omega < \omega_0 \\ \varepsilon_{\text{eq}} \frac{\omega}{\omega_0} + \sqrt{\max \varepsilon_N^2 + \alpha \max \varepsilon_T^2} \left(1 - \frac{\omega}{\omega_0} \right) & \omega_0 \leq \omega < \omega_0 \\ \sqrt{\max \varepsilon_N^2 + \alpha \max \varepsilon_T^2} & \omega \geq \omega_0 \end{cases} \quad (55)$$

	material parameter	symbol	value	units
mechanics	normal elastic constant	E_0	21.5	GPa
	tangential/normal stiffness ratio	α	0.3	-
	tensile strength	f_t	2.1	MPa
	tensile fracture energy	G_t	50	J/m ²
mass transport	capacity	c	1.62×10^{-8}	s ² /m ²
	density	ρ_{w0}	1000	kg/m ³
	permeability	κ	5×10^{-18}	m ²
	viscosity	μ	8.9×10^{-4}	Pa·s
	reference pressure	p_0	0 or 1	MPa
coupling	crack tortuosity	ξ	1	-
	bulk modulus	K_w	2.15	GPa
	Biot coefficient	b	0–1	-

Table 1: Material parameters used in the verification examples. Approximate values of macroscopic elastic modulus, E , and Poisson’s ratio, ν , are estimated by analyses of the RVE response as 13.97 GPa and 0.175, respectively. Macroscopic RVE permeability coefficient of the intact material is exactly equal to the microscopic one, i.e., $\rho_{w0}\kappa/\mu = 5.618 \times 10^{-12}$ s.

with ω_0 being the direction at which both branches of Eq. (53) are equal.

The initial slope of the strain softening, K , is defined using K_t and K_s , the slopes for pure tension and shear, respectively. These are dependent on contact length l and read

$$K_t = \frac{2E_0 f_t^2 l}{2E_0 G_t - f_t^2 l} \quad K_s = \frac{18\alpha E_0 f_t^2 l}{32\alpha E_0 G_t - 9f_t^2 l} \quad (56)$$

Finally, parameter n_t reads

$$n_t = \frac{\ln(K_t/(K_t - K_s))}{\ln(1 - 2\omega_0/\pi)} \quad (57)$$

If the confinement effect is included, the constitutive model features also the volumetric strain, which, after expansion, would appear through its macroscopic (slow) component and microscopic (fast) component evaluated at the RVE from Delaunay tetrahedrons according to Appendix D.

Transport constitutive equation relates the scalar flux, j , and the scalar pressure gradient, g : $j = f_j(p, g, \delta_N)$. It is assumed to be in a form $j = -\lambda(p, \delta_N)g$, flux is linearly dependent on pressure gradient. λ is material permeability coefficient dependent on pressure p and crack opening δ_N . For sake of simplicity, the effect of pressure is not considered here even though the homogenization derivation assumes such dependency. Reader is referred to paper [29] where the pressure dependent permeability coefficient is used in the studies with the *homogenized* and *full* model. The crack opening dependence is adopted from Ref. [39] as a summation of permeability coefficient of intact material and an effect of cracks

$$\lambda = \frac{\rho_{w0}\kappa}{\mu} + \frac{\xi\rho_{w0}}{12\mu S} \sum_{i=1}^3 \delta_{Ni}^3 l_{ci} \quad (58)$$

ρ_{w0} is fluid density, κ is permeability, μ is viscosity, ξ is crack tortuosity parameter, δ_N and l_c are normal crack openings and crack lengths of associated mechanical elements, see Ref. [39] for details.

Material parameters used throughout the paper are listed in Tab. 1. These parameters were partly taken from literature and partly identified by simulating Brazilian test followed by measurement of water flux through the cracked specimens according to Refs. [72, 3].

F Analytical solution to the Terzaghi's consolidation problem

Analytical solutions [66, 23] to the elastic Terzaghi's consolidation problems (pressure and traction loading) are the following

$$\text{loading by pressure} \quad p(\chi, \tau) = p^* F_1(\chi, \tau) \quad u(\chi, \tau) = -\frac{p^* \Upsilon L}{G} F_2(\chi, \tau) \quad (59)$$

$$\text{loading by traction} \quad p(\chi, \tau) = \frac{t_x^* \Upsilon L}{GS} [1 - F_1(\chi, \tau)] \quad u(\chi, \tau) = t_x^* L \left[\frac{(1 - 2\nu_u)(1 - \chi)}{2G(1 - \nu_u)} + \frac{(\nu_u - \nu)F_2(\chi, \tau)}{2G(1 - \nu)(1 - \nu_u)} \right] \quad (60)$$

where functions F_1 and F_2 read

$$F_1(\chi, \tau) = 1 - \sum_{m=1,3,\dots}^{\infty} \frac{4}{m\pi} \sin\left(\frac{m\pi\chi}{2}\right) \exp(-m^2\pi^2\tau) \quad (61)$$

$$F_2(\chi, \tau) = \sum_{m=1,3,\dots}^{\infty} \frac{8}{m^2\pi^2} \cos\left(\frac{m\pi\chi}{2}\right) [1 - \exp(-m^2\pi^2\tau)] \quad (62)$$

$\chi = x/L$, $\tau = \lambda t/4CL^2$, $\Upsilon = b(1 - 2\nu)/[2(1 - \nu)]$, $L = \text{prism length} = 0.5 \text{ m}$, $G = E/2(1 + \nu)$, $C = (1 - \nu_u)(1 - 2\nu)/[M_b(1 - \nu)(1 - 2\nu_u)]$, $M_b = 1/c$, $\nu_u = (3K_u - 2G)/2(3K_u + G)$ and $K_u = M_b b^2 + E/3(1 - 2\nu)$.

G Analytical solution to the elastic pressurized hollow cylinder problem

Grassl et al. [37] derived analytical solution for the steady state elastic problem in terms of pressure p and radial displacement u_r .

$$p(r) = p_i \frac{\ln \frac{r_o}{r}}{\ln \frac{r_o}{r_i}} \quad (63)$$

$$u_r(r) = -\frac{p_i b}{E} \frac{1 - \nu^2}{2} \left[\frac{r_o^2}{r_o^2 - r_i^2} \left(\frac{r_o^2(1 + \nu)}{r(1 - \nu)} + r \right) + r \frac{\frac{1}{1 + \nu} - \ln \frac{r}{r_i}}{\ln \frac{r_o}{r_i}} \right] - \frac{p_i(1 - b)}{E} \frac{r_o^2 r_i^2}{r_o^2 - r_i^2} \left(\frac{1 + \nu}{r} + \frac{r(1 - \nu)}{r_o^2} \right) \quad (64)$$

r is the radial coordinate, p_i is the internal pressure, r_i and r_o are internal and external radii.

Acknowledgements

Jan Eliáš gratefully acknowledges financial support from the Czech Science Foundation under project no. GA19-12197S.

References

- [1] Mohammed Abdellatef and Mohammed Alnaggar. "Energy-Based Coarse Graining of the Lattice-Discrete Particle Model". In: *Journal of Engineering Mechanics* 146.5 (2020), p. 04020026. DOI: 10.1061/(ASCE)EM.1943-7889.0001743.
- [2] S.E. Alavi, J.F. Ganghoffer, H. Reda, and M. Sadighi. "Construction of micromorphic continua by homogenization based on variational principles". In: *Journal of the Mechanics and Physics of Solids* 153 (2021), p. 104278. ISSN: 0022-5096. DOI: 10.1016/j.jmps.2020.104278.
- [3] C.M. Aldea, S.P. Shah, and A. Karr. "Permeability of cracked concrete". In: *Materials and Structures* 32 (1999), pp. 370–376. ISSN: 1359-5997. DOI: 10.1007/BF02479629.
- [4] Mohammed Alnaggar, Gianluca Cusatis, and Giovanni Di Luzio. "Lattice Discrete Particle Modeling (LDPM) of Alkali Silica Reaction (ASR) deterioration of concrete structures". In: *Cement and Concrete Composites* 41 (2013), pp. 45–59. ISSN: 0958-9465. DOI: 10.1016/j.cemconcomp.2013.04.015.

- [5] Mohammed Alnaggar, Daniele Pelessone, and Gianluca Cusatis. “Lattice Discrete Particle Modeling of Reinforced Concrete Flexural Behavior”. In: *Journal of Structural Engineering* 145.1 (2019), p. 04018231. DOI: 10.1061/(ASCE)ST.1943-541X.0002230.
- [6] Daisuke Asahina, Pengzhi Pan, Kimikazu Tsusaka, Mikio Takeda, and John E. Bolander. “Simulating hydraulic fracturing processes in laboratory-scale geological media using three-dimensional TOUGH-RBSN”. In: *Journal of Rock Mechanics and Geotechnical Engineering* 10.6 (2018), pp. 1102–1111. ISSN: 1674-7755. DOI: 10.1016/j.jrmge.2018.09.001.
- [7] Ignatios Athanasiadis, Simon J. Wheeler, and Peter Grassl. “Hydro-mechanical network modelling of particulate composites”. In: *International Journal of Solids and Structures* 130-131 (2018), pp. 49–60. ISSN: 0020-7683. DOI: 10.1016/j.ijsolstr.2017.10.017.
- [8] A. Bensoussan, J.-L. Lions, and G. Papanicolaou. *Asymptotic Analysis for Periodic Structures*. North-Holland, 1978.
- [9] Maurice A. Biot. “General Theory of Three-Dimensional Consolidation”. In: *Journal of Applied Physics* 12.2 (1941), pp. 155–164. DOI: 10.1063/1.1712886.
- [10] J.E. Bolander and S. Berton. “Simulation of shrinkage induced cracking in cement composite overlays”. In: *Cement and Concrete Composites* 26.7 (2004), pp. 861–871. ISSN: 0958-9465. DOI: 10.1016/j.cemconcomp.2003.04.001.
- [11] John E. Bolander, Jan Eliáš, Gianluca Cusatis, and Kohei Nagai. “Discrete mechanical models of concrete fracture”. In: *Engineering Fracture Mechanics* 257 (2021), p. 108030. ISSN: 0013-7944. DOI: 10.1016/j.engfracmech.2021.108030.
- [12] Sandra Carstens and Detlef Kuhl. “Higher-order accurate implicit time integration schemes for transport problems”. In: *Archive of Applied Mechanics* 82.8 (2012), pp. 1007–1039. ISSN: 1432-0681. DOI: 10.1007/s00419-012-0638-0.
- [13] C. Ceccato, X. Zhou, D. Pelessone, and G. Cusatis. “Proper Orthogonal Decomposition Framework for the Explicit Solution of Discrete Systems With Softening Response”. In: *Journal of Engineering Mechanics* 85.5 (2018), p. 051004. DOI: 10.1115/1.4038967.
- [14] Le Chen, Weiwei Sun, Bingcheng Chen, Ze Shi, Jianzhong Lai, and Jun Feng. “Multiscale study of fibre orientation effect on pullout and tensile behavior of steel fibre reinforced concrete”. In: *Construction and Building Materials* 283 (2021), p. 122506. ISSN: 0950-0618. DOI: 10.1016/j.conbuildmat.2021.122506.
- [15] Peter Yichen Chen, Maytee Chantharayukhonthorn, Yonghao Yue, Eitan Grinspun, and Ken Kamrin. “Hybrid discrete-continuum modeling of shear localization in granular media”. In: *Journal of the Mechanics and Physics of Solids* 153 (2021), p. 104404. ISSN: 0022-5096. DOI: 10.1016/j.jmps.2021.104404.
- [16] E.W.C. Coenen, V.G. Kouznetsova, E. Bosco, and M.G.D. Geers. “A multi-scale approach to bridge microscale damage and macroscale failure: a nested computational homogenization-localization framework”. In: *International Journal of Fracture* 178 (2012), pp. 157–178. DOI: 10.1007/s10704-012-9765-4.
- [17] E.W.C. Coenen, V.G. Kouznetsova, and M.G.D. Geers. “Novel boundary conditions for strain localization analyses in microstructural volume elements”. In: *International Journal for Numerical Methods in Engineering* 90.1 (2012), pp. 1–21. DOI: 10.1002/nme.3298.
- [18] A. Corigliano, M. Dossi, and S. Mariani. “Model Order Reduction and domain decomposition strategies for the solution of the dynamic elastic-plastic structural problem”. In: *Computer Methods in Applied Mechanics and Engineering* 290 (2015), pp. 127–155. ISSN: 0045-7825. DOI: 10.1016/j.cma.2015.02.021.
- [19] Alejandro Cornejo, Vicente Mataix, Francisco Zárata, and Eugenio Oñate. “Combination of an adaptive remeshing technique with a coupled FEM-DEM approach for analysis of crack propagation problems”. In: *Computational Particle Mechanics* 7 (2020), pp. 735–752. DOI: 10.1007/s40571-019-00306-4.
- [20] Gianluca Cusatis and Luigi Cedolin. “Two-scale study of concrete fracturing behavior”. In: *Engineering Fracture Mechanics* 74.1 (2007). Fracture of Concrete Materials and Structures, pp. 3–17. ISSN: 0013-7944. DOI: 10.1016/j.engfracmech.2006.01.021.
- [21] Gianluca Cusatis, Andrea Mencarelli, Daniele Pelessone, and James Baylot. “Lattice discrete particle model (LDPM) for failure behavior of concrete. II: Calibration and validation”. In: *Cement and Concrete composites* 33.9 (2011), pp. 891–905.

- [22] Gianluca Cusatis, Daniele Pelessone, and Andrea Mencarelli. “Lattice Discrete Particle Model (LDPM) for failure behavior of concrete. I: Theory”. In: *Cement and Concrete Composites* 33.9 (2011), pp. 881–890. ISSN: 0958-9465. DOI: 10.1016/j.cemconcomp.2011.02.011.
- [23] E. Detournay and A. H.-D. Cheng. “Fundamentals of Poroelasticity”. In: *Analysis and Design Methods*. Ed. by Charles Fairhurst. Oxford: Pergamon, 1993, pp. 113–171. ISBN: 978-0-08-040615-2. DOI: 10.1016/B978-0-08-040615-2.50011-3.
- [24] Emmanuel Detournay and Alexander H.-D. Cheng. “Comprehensive Rock Engineering: Principles, Practice & Projects”. In: vol. II. 1995, pp. 113–171. DOI: 10.1016/B978-0-08-040615-2.50011-3.
- [25] Jan Eliáš. “Adaptive technique for discrete models of fracture”. In: *International Journal of Solids and Structures* 100–101 (2016), pp. 376–387. ISSN: 0020-7683. DOI: 10.1016/j.ijsolstr.2016.09.008.
- [26] Jan Eliáš. “Boundary Layer Effect on Behavior of Discrete Models”. In: *Materials* 10 (2017), p. 157. ISSN: 1996-1944. DOI: 10.3390/ma10020157.
- [27] Jan Eliáš. “Elastic properties of isotropic discrete systems: Connections between geometric structure and Poisson’s ratio”. In: *International Journal of Solids and Structures* 191–192 (2020), pp. 254–263. ISSN: 0020-7683. DOI: 10.1016/j.ijsolstr.2019.12.012.
- [28] Jan Eliáš and Miroslav Vořechovský. “Fracture in random quasibrittle media: I. Discrete mesoscale simulations of load capacity and fracture process zone”. In: *Engineering Fracture Mechanics* 235 (2020), p. 107160. ISSN: 0013-7944. DOI: 10.1016/j.engfracmech.2020.107160.
- [29] Jan Eliáš, Hao Yin, and Gianluca Cusatis. “Homogenization of discrete diffusion models by asymptotic expansion”. In: *International Journal for Numerical and Analytical Methods in Geomechanics* (2022). under review. ISSN: 0363-9061.
- [30] Caroline Fahy, Simon J. Wheeler, Domenico Gallipoli, and Peter Grassl. “Corrosion induced cracking modelled by a coupled transport-structural approach”. In: *Cement and Concrete Research* 94 (2017), pp. 24–35. ISSN: 0008-8846. DOI: 10.1016/j.cemconres.2017.01.007.
- [31] Jun Feng, Meili Song, Qiang He, Weiwei Sun, Lei Wang, and Kaijing Luo. “Numerical study on the hard projectile perforation on RC panels with LDPM”. In: *Construction and Building Materials* 183 (2018), pp. 58–74. ISSN: 0950-0618. DOI: 10.1016/j.conbuildmat.2018.06.020.
- [32] Jacob Fish, Wen Chen, and Renge Li. “Generalized mathematical homogenization of atomistic media at finite temperatures in three dimensions”. In: *Computer Methods in Applied Mechanics and Engineering* 196.4 (2007), pp. 908–922. ISSN: 0045-7825. DOI: 10.1016/j.cma.2006.08.001.
- [33] Jacob Fish, Kamlun Shek, Muralidharan Pandheeradi, and Mark S. Shephard. “Computational plasticity for composite structures based on mathematical homogenization: Theory and practice”. In: *Computer Methods in Applied Mechanics and Engineering* 148.1 (1997), pp. 53–73. ISSN: 0045-7825. DOI: 10.1016/S0045-7825(97)00030-3.
- [34] William B. Fuller and Sanford E. Thompson. “The Laws of Proportioning Concrete”. In: *Transactions of the American Society of Civil Engineers* 59.2 (1907), pp. 67–143. DOI: 10.1061/TACEAT.0001979.
- [35] Somnath Ghosh, Kyunghoon Lee, and Prasanna Raghavan. “A multi-level computational model for multi-scale damage analysis in composite and porous materials”. In: *International Journal of Solids and Structures* 38.14 (2001), pp. 2335–2385. ISSN: 0020-7683. DOI: 10.1016/S0020-7683(00)00167-0.
- [36] I.M. Gitman, H. Askes, and L.J. Sluys. “Representative volume: Existence and size determination”. In: *Engineering Fracture Mechanics* 74.16 (2007), pp. 2518–2534. ISSN: 0013-7944. DOI: 10.1016/j.engfracmech.2006.12.021.
- [37] P. Grassl, C. Fahy, D. Gallipoli, and S.J. Wheeler. “On a 2D hydro-mechanical lattice approach for modelling hydraulic fracture”. In: *Journal of the Mechanics and Physics of Solids* 75 (2015), pp. 104–118. ISSN: 0022-5096. DOI: 10.1016/j.jmps.2014.11.011.
- [38] Peter Grassl. “A lattice approach to model flow in cracked concrete”. In: *Cement and Concrete Composites* 31.7 (2009), pp. 454–460. ISSN: 0958-9465. DOI: 10.1016/j.cemconcomp.2009.05.001.
- [39] Peter Grassl and John Bolander. “Three-Dimensional Network Model for Coupling of Fracture and Mass Transport in Quasi-Brittle Geomaterials”. In: *Materials* 9.9 (2016), p. 782. ISSN: 1996-1944. DOI: 10.3390/ma9090782.

- [40] *Homogenization of Coupled Phenomena in Heterogenous Media*. John Wiley & Sons, Ltd, 2009, pp. 1–476. ISBN: 9780470612033. DOI: 10.1002/9780470612033.
- [41] M. Horák, B. Patzák, and M. Jirásek. “On design of element evaluators in OOFEM”. In: *Advances in Engineering Software* 72 (2014), pp. 193–202. ISSN: 0965-9978. DOI: 10.1016/j.advengsoft.2014.01.006.
- [42] Kenneth E. Jansen, Christian H. Whiting, and Gregory M. Hulbert. “A generalized- α method for integrating the filtered Navier–Stokes equations with a stabilized finite element method”. In: *Computer Methods in Applied Mechanics and Engineering* 190.3 (2000), pp. 305–319. ISSN: 0045-7825. DOI: 10.1016/S0045-7825(00)00203-6.
- [43] Congrui Jin, Nicola Buratti, Marco Stacchini, Marco Savoia, and Gianluca Cusatis. “Lattice discrete particle modeling of fiber reinforced concrete: Experiments and simulations”. In: *European Journal of Mechanics - A/Solids* 57 (2016), pp. 85–107. ISSN: 0997-7538. DOI: 10.1016/j.euromechsol.2015.12.002.
- [44] P. Kerfriden, J. C. Passieux, and S. P. A. Bordas. “Local/global model order reduction strategy for the simulation of quasi-brittle fracture”. In: *International Journal for Numerical Methods in Engineering* 89.2 (2012), pp. 154–179. DOI: <https://doi.org/10.1002/nme.3234>.
- [45] V.G. Kouznetsova, M.G.D. Geers, and W.A.M. Brekelmans. “Multi-scale second-order computational homogenization of multi-phase materials: a nested finite element solution strategy”. In: *Computer Methods in Applied Mechanics and Engineering* 193.48 (2004), pp. 5525–5550. ISSN: 0045-7825. DOI: 10.1016/j.cma.2003.12.073.
- [46] Erol Lale, Roozbeh Rezakhani, Mohammed Alnaggar, and Gianluca Cusatis. “Homogenization coarse graining (HCG) of the lattice discrete particle model (LDPM) for the analysis of reinforced concrete structures”. In: *Engineering Fracture Mechanics* 197 (2018), pp. 259–277. ISSN: 0013-7944. DOI: 10.1016/j.engfracmech.2018.04.043.
- [47] Mathias Lebihain, Laurent Ponson, Djimédo Kondo, and Jean-Baptiste Leblond. “Effective toughness of disordered brittle solids: A homogenization framework”. In: *Journal of the Mechanics and Physics of Solids* 153 (2021), p. 104463. ISSN: 0022-5096. DOI: 10.1016/j.jmps.2021.104463.
- [48] Weixin Li, Xinwei Zhou, J. William Carey, Luke P. Frash, and Gianluca Cusatis. “Multiphysics Lattice Discrete Particle Modeling (M-LDPM) for the Simulation of Shale Fracture Permeability”. In: *Rock Mechanics and Rock Engineering* 51 (2018), pp. 3963–3981. ISSN: 0723-2632. DOI: 10.1007/s00603-018-1625-8.
- [49] Christian Miehe, Steffen Mauthe, and Stephan Teichtmeister. “Minimization principles for the coupled problem of Darcy–Biot-type fluid transport in porous media linked to phase field modeling of fracture”. In: *Journal of the Mechanics and Physics of Solids* 82 (2015), pp. 186–217. ISSN: 0022-5096. DOI: 10.1016/j.jmps.2015.04.006.
- [50] Florian Müller-Plathe. “Coarse-Graining in Polymer Simulation: From the Atomistic to the Mesoscopic Scale and Back”. In: *ChemPhysChem* 3.9 (2002), pp. 754–769. DOI: 10.1002/1439-7641(20020916)3:9<754::AID-CPHC754>3.0.CO;2-U.
- [51] J. Oliver, M. Caicedo, E. Roubin, A.E. Huespe, and J.A. Hernández. “Continuum approach to computational multiscale modeling of propagating fracture”. In: *Computer Methods in Applied Mechanics and Engineering* 294 (2015), pp. 384–427. ISSN: 0045-7825. DOI: 10.1016/j.cma.2015.05.012.
- [52] Niels Saabye Ottosen. “A Failure Criterion for Concrete”. In: *Journal of the Engineering Mechanics Division ASCE* 103 (1977), pp. 527–535. ISSN: 0044-7951. DOI: 10.1061/JMCEA3.0002248.
- [53] Saeed Rahimi-Aghdam, Viet-Tuan Chau, Hyunjin Lee, Hoang Nguyen, Weixin Li, Satish Karra, Esteban Rougier, Hari Viswanathan, Gowri Srinivasan, and Zdeněk P. Bažant. “Branching of hydraulic cracks enabling permeability of gas or oil shale with closed natural fractures”. In: *Proceedings of the National Academy of Sciences* 116.5 (2019), pp. 1532–1537. ISSN: 0027-8424. DOI: 10.1073/pnas.1818529116.
- [54] Guotong Ren and Rami M. Younis. “An integrated numerical model for coupled poro-hydro-mechanics and fracture propagation using embedded meshes”. In: *Computer Methods in Applied Mechanics and Engineering* 376 (2021), p. 113606. ISSN: 0045-7825. DOI: 10.1016/j.cma.2020.113606.
- [55] Roozbeh Rezakhani, Mohammed Alnaggar, and Gianluca Cusatis. “Multiscale Homogenization Analysis of Alkali–Silica Reaction (ASR) Effect in Concrete”. In: *Engineering* 5.6 (2019), pp. 1139–1154. ISSN: 2095-8099. DOI: 10.1016/j.eng.2019.02.007.
- [56] Roozbeh Rezakhani and Gianluca Cusatis. “Asymptotic expansion homogenization of discrete fine-scale models with rotational degrees of freedom for the simulation of quasi-brittle materials”. In: *Journal of the Mechanics and Physics of Solids* 88 (2016), pp. 320–345. ISSN: 0022-5096. DOI: 10.1016/j.jmps.2016.01.001.

- [57] Roozbeh Rezakhani, Xinwei Zhou, and Gianluca Cusatis. “Adaptive multiscale homogenization of the lattice discrete particle model for the analysis of damage and fracture in concrete”. In: *International Journal of Solids and Structures* 125 (2017), pp. 50–67. ISSN: 0020-7683. DOI: [h10.1016/j.ijsolstr.2017.07.016](https://doi.org/10.1016/j.ijsolstr.2017.07.016).
- [58] O. Rokoš, R. H. J. Peerlings, J. Zeman, and L. A. A. Beex. “An adaptive variational Quasicontinuum methodology for lattice networks with localized damage”. In: *International Journal for Numerical Methods in Engineering* 112.2 (2017), pp. 174–200. DOI: [10.1002/nme.5518](https://doi.org/10.1002/nme.5518).
- [59] J. Saliba, M. Matallah, A. Loukili, J.P. Regoin, D. Grégoire, L. Verdon, and G. Pijaudier-Cabot. “Experimental and numerical analysis of crack evolution in concrete through acoustic emission technique and mesoscale modelling”. In: *Engineering Fracture Mechanics* 167 (2016), pp. 123–137. ISSN: 0013-7944. DOI: [10.1016/j.engfracmech.2016.03.044](https://doi.org/10.1016/j.engfracmech.2016.03.044).
- [60] Lei Shen, Weixin Li, Xinwei Zhou, Jun Feng, Giovanni Di Luzio, Qingwen Ren, and Gianluca Cusatis. “Multi-physics Lattice Discrete Particle Model for the simulation of concrete thermal spalling”. In: *Cement and Concrete Composites* 106 (2020), p. 103457. ISSN: 0958-9465. DOI: [10.1016/j.cemconcomp.2019.103457](https://doi.org/10.1016/j.cemconcomp.2019.103457).
- [61] Lawrence Sirovich. “Turbulence and the dynamics of coherent structures part I: coherent structures”. In: *Quarterly of Applied Mathematics* 45.3 (1987), pp. 561–571. ISSN: 1552-4485. DOI: [10.2307/43637457](https://doi.org/10.2307/43637457).
- [62] R.J.M. Smit, W.A.M. Brekelmans, and H.E.H. Meijer. “Prediction of the mechanical behavior of nonlinear heterogeneous systems by multi-level finite element modeling”. In: *Computer Methods in Applied Mechanics and Engineering* 155.1 (1998), pp. 181–192. ISSN: 0045-7825. DOI: [10.1016/S0045-7825\(97\)00139-4](https://doi.org/10.1016/S0045-7825(97)00139-4).
- [63] Jovanca Smith, Gianluca Cusatis, Daniele Pelessone, Eric Landis, James O’Daniel, and James Baylot. “Discrete modeling of ultra-high-performance concrete with application to projectile penetration”. In: *International Journal of Impact Engineering* 65 (2014), pp. 13–32. ISSN: 0734-743X. DOI: [10.1016/j.ijimpeng.2013.10.008](https://doi.org/10.1016/j.ijimpeng.2013.10.008).
- [64] Jan Stránský and Milan Jirásek. “Calibration of particle-based models using cells with periodic boundary conditions”. In: *II International Conference on Particle-based Methods - Fundamentals and Applications*. 2011, pp. 1–12.
- [65] Hongxiang Tang, Yan Dong, Ting Wang, and Yifeng Dong. “Simulation of strain localization with discrete element-Cosserat continuum finite element two scale method for granular materials”. In: *Journal of the Mechanics and Physics of Solids* 122 (2019), pp. 450–471. ISSN: 0022-5096. DOI: [10.1016/j.jmps.2018.09.029](https://doi.org/10.1016/j.jmps.2018.09.029).
- [66] K. Terzaghi. “Die Berechnung der Durchlässigkeitsziffer des Tones aus Dem Verlauf der Hidrodynamischen Spannungerscheinungen Akademie der Wissenschaften in Wien”. In: *Mathematisch-Naturwissen-Schaftliche Klasse* 132 (1925), pp. 125–138.
- [67] Sergio Turteltaub, Niels van Hoorn, Wim Westbroek, and Christian Hirsch. “Multiscale analysis of mixed-mode fracture and effective traction-separation relations for composite materials”. In: *Journal of the Mechanics and Physics of Solids* 117 (2018), pp. 88–109. ISSN: 0022-5096. DOI: [10.1016/j.jmps.2018.04.009](https://doi.org/10.1016/j.jmps.2018.04.009).
- [68] Ole Ivar Ulven and WaiChing Sun. “Capturing the two-way hydromechanical coupling effect on fluid-driven fracture in a dual-graph lattice beam model”. In: *International Journal for Numerical and Analytical Methods in Geomechanics* 42.5 (2018), pp. 736–767. DOI: [10.1002/nag.2763](https://doi.org/10.1002/nag.2763).
- [69] Jörg F. Unger. “An FE2-X1 approach for multiscale localization phenomena”. In: *Journal of the Mechanics and Physics of Solids* 61.4 (2013), pp. 928–948. ISSN: 0022-5096. DOI: [10.1016/j.jmps.2012.12.010](https://doi.org/10.1016/j.jmps.2012.12.010).
- [70] M. Th. van Genuchten. “A Closed-form Equation for Predicting the Hydraulic Conductivity of Unsaturated Soils”. In: *Soil Science Society of America Journal* 44.5 (1980), pp. 892–898. DOI: [10.2136/sssaj1980.03615995004400050002x](https://doi.org/10.2136/sssaj1980.03615995004400050002x).
- [71] Cong Wang, Zhaoqin Huang, and Yu-Shu Wu. “Coupled numerical approach combining X-FEM and the embedded discrete fracture method for the fluid-driven fracture propagation process in porous media”. In: *International Journal of Rock Mechanics and Mining Sciences* 130 (2020), p. 104315. ISSN: 1365-1609. DOI: [10.1016/j.ijrmms.2020.104315](https://doi.org/10.1016/j.ijrmms.2020.104315).
- [72] Kejin Wang, Daniel C. Jansen, Surendra P. Shah, and Alan F. Karr. “Permeability study of cracked concrete”. In: *Cement and Concrete Research* 27.3 (1997), pp. 381–393. ISSN: 0008-8846. DOI: [10.1016/S0008-8846\(97\)00031-8](https://doi.org/10.1016/S0008-8846(97)00031-8).
- [73] Zachary A. Wilson and Chad M. Landis. “Phase-field modeling of hydraulic fracture”. In: *Journal of the Mechanics and Physics of Solids* 96 (2016), pp. 264–290. ISSN: 0022-5096. DOI: [10.1016/j.jmps.2016.07.019](https://doi.org/10.1016/j.jmps.2016.07.019).

- [74] Okan Yilmaz and Jean-François Molinari. “A mesoscale fracture model for concrete”. In: *Cement and Concrete Research* 97 (2017), pp. 84–94. ISSN: 0008-8846. DOI: 10.1016/j.cemconres.2017.03.014.